Published in Journal of Hydrology 399, issues 1-2, 29-47, 2011
which should be used for any reference to this work

Process-based groundwater salinisation risk assessment methodology: Application to the Akrotiri aquifer (Southern Cyprus)

Ellen Milnes

Centre d'hydrogéologie, Université de Neuchâtel, Rue Emile Argand 11, CP 158, 2009-Neuchâtel, Switzerland

SUMMARY

Groundwater salinisation is a major groundwater contamination issue world-wide and can be caused by different processes, such as seawater intrusion, agrochemical pollution, geogenic contamination and irrigation-induced salinisation. In many areas, several salinisation processes are superimposed. Since remedial measures vary for different salinisation processes, correct identification is fundamental for adequate design of management strategies: different strategies may be required in one and the same aquifer, depending on which salinisation process is active where in the domain.

A simulation-based salinisation risk assessment methodology is proposed, based on the principle of linear superposition of total dissolved solutes in groundwater. In a first step, the measured bulk salinity distribution is used to calibrate a numerical groundwater flow and transport model, accounting for all identified salinisation processes. Then, the bulk salinity distribution is decomposed into different salinity components by adapting the boundary conditions, running a simulation for each salinisation process separately. These simulation results yield the necessary components to calculate the risk index distributions, which are a measure of the respective future potential salinity increase. Overlaying the risk index distributions with a defined threshold concentration reveals risk areas requiring remediation or conservation measures with respect to each process. The risk area maps resulting from this methodology are a promising tool for the design of groundwater management schemes. They condense relevant information from complex dynamic processes obtained from numerical simulations and visualise the results in simple and static maps, accessible to decision makers who are not familiar with groundwater dynamics.

The different steps of the salinisation risk assessment procedure are first described and illustrated on a synthetic example and then applied to a real aquifer system in Southern Cyprus (Akrotiri), where three major salinisation processes are superimposed.

Keywords

Risk assessment, Groundwater salinisation, Transport modelling, Seawater intrusion, Irrigation salinity, Cyprus

1. Introduction

Salinisation is a wide-spread threat to fresh groundwater resources and can be considered as one of the most prominent global groundwater pollution problems. In contrast to specific pollutants, salinity as such is not a contaminant but is merely a measure of the content of dissolved solutes. Its contamination potential and toxicity (e.g. to plants) is related to an overall concentration threshold of dissolved solutes and not to specific constituents of the water composition. Salinity may have many different origins and can either be caused by primary salinisation processes that actually add solutes to the system, such as seawater intrusion, dissolution of geogenic salt deposits or agricultural inputs (e.g. Konikow and Person, 1985; Custodio, 1997; Sites and Kraft, 2000; Pearce and Schumann, 2001). Or, it can be induced by secondary salinisation, such as solute recycling from irrigation or by evaporative processes: secondary processes do not add any solutes to the system, but lead to salinisation by redistribution or concentration of solutes already present in the system (Milnes and Renard, 2004; Milnes and Perrochet, 2006).

In areas affected by groundwater salinisation, correct identification of the spatial distribution and dynamic interplay of the superimposed salinity components is crucial, since the respective remedial or conservation measures may be entirely different. To avoid seawater intrusion, as an example, the water table has to be kept high, while to avoid irrigation-induced salinisation the groundwater table should be kept low. In many coastal irrigated aquifers, in particular in the Mediterranean region, these two salinisation processes are often superimposed.

Identification of different origins of salinisation can be considered a separate field in hydrogeological research and is efficiently addressed by means of various hydrogeochemical techniques (e.g. Richter and Kreidtler, 1993; Vengosh and Rosenthal, 1994; Custodio, 1997; Vengosh et al., 1999). As opposed to simple salinity measurements, sophisticated techniques that yield clear information about the origin of salinity are time-consuming and costly,

E-mail address: ellen.milnes@unine.ch

and usually only yield snap-shots in time and space. Hence, combining information on the origins of salinity from such investigations with numerical simulations is a promising strategy, not only to investigate the dynamic interplay of different salinisation processes, but also to decompose the bulk salinity evolution into different salinity components induced by different processes.

Vulnerability and risk assessments are becoming a standard approach in groundwater management when dealing with water quality and contamination issues. Vulnerability maps are designed to identify areas of greatest potential for groundwater contamination on the basis of hydrogeological criteria, while groundwater risk assessments additionally consider the presence of potential contamination sources or polluting land-use activities (Gogu and Dassargues, 2000). The most commonly used vulnerability mapping procedures are based on empirical point rating systems, such as DRASTIC (Aller et al., 1987), EPIK (Doerfliger and Zwahlen, 1997), GOD (Foster, 1987) or SINTACS (Civita and de Rigibus, 1995), bringing together key factors which influence the solute transport process. However, it has been found that the vulnerability of aquifers to groundwater contamination can rarely be predicted with these key factors (e.g. Ruppert, 2001). Gogu and Dassargues (2000) therefore emphasize the need for physically based risk and vulnerability assessments. Such an example is presented by Stewartd and Loague (1999), who developed a regional-scale vulnerability assessment methodology to estimate the impact of non-point source groundwater contamination, using a generalised type transfer function. Sophocleous and Ma (1998) used numerical modelling combined with sensitivity analysis multiple regression analysis and classification procedures to develop a decision support model to assess spatial vulnerability to groundwater salinisation in the Great Bend Prairie aquifer of Kansas. Another example of a physically-based approach is given in Connell and van den Daele (2003), who investigated the use of analytical solutions for unsaturated solute migration, in order to calculate contaminant transport to groundwater in view of combining it with a geographic information system (GIS) to establish vulnerability maps. The spatial overlay principle of different information is common to most approaches, yielding vulnerability or risk maps, which can be used by decision makers. The overlay principle is also used in the present approach. However, the information which is overlain is entirely deduced from numerical flow and transport simulations: the spatial distribution of the information is therefore continuous.

Hence, the aim of this work is to present a physically based salinisation risk mapping procedure and to apply it to a real-case site. The calibrated observed (bulk) salinity distribution is decomposed, which means 'picked apart', in contrast to the common usage of the word decomposed, into several salinity components, by adapting the boundary conditions in a flow and transport model, assuming linear superposition of total dissolved solids with different origins. The decomposed salinity distributions are then used in a simple overlay principle to calculate the respective spatial risk index distributions, with which areas are identified that are prone to further salinisation. The salinisation risk index mapping procedure is first illustrated on a schematic 2D model and then applied to a real-case site in Southern Cyprus (Akrotiri aquifer) using a 3D finite element model, revealing the practical outcomes of the method, but also the limitations.

2. Definition of the risk index $R_i(x)$

The basis of risk assessments is the comparison of a present state of the environment with an adverse state which may potentially occur in the future, a state which will have a negative impact on human interests (e.g. Helm, 1996). Placing this general definition into the context of groundwater salinisation requires first of all definition of an 'adverse state' for each salinisation process in an aquifer system.

For any salinisation process we may be dealing with, the 'adverse state' with respect to the ith of n salinisation processes is defined here as the steady-state salinity $C_i(\boldsymbol{x}, \infty)$ in response to a given hydraulic condition, with $\boldsymbol{x}$ symbolising the Cartesian coordinates in 1, 2 or 3 dimensions. The 'adverse state' of the ith salinisation process reflects the direction towards which the system is heading, being the 'worst case' for a given hydraulic setting. Hence, the difference between the salinity $C_i(\boldsymbol{x}, t_p)$ at 'present state' t_p, and the respective steady-state salinity $C_i(\boldsymbol{x}, \infty)$ yields the potential future salinity increase with respect to the ith salinisation process. Since all the following evaluations are entirely based on deterministic model simulations, while risk assessments are generally related to probabilistic calculations, we will not define a 'probability' or risk of the 'adverse state' actually occurring, but will define a risk index. This salinisation risk index, denoted $R_i(\boldsymbol{x})$, in response to the ith salinisation process at any point $\boldsymbol{x}$ in the domain is a measure of the future potential magnitude of salinity increase and is defined as follows:

$$R_i(\boldsymbol{x}) = \frac{C_i(\boldsymbol{x}, \infty) - C_i(\boldsymbol{x}, t_p)}{C_B(\boldsymbol{x}, \infty)} \tag{1}$$

with $C_i(\boldsymbol{x}, \infty)$ being the steady-state salinity induced by the ith salinisation process at a point $\boldsymbol{x}$ for a given hydraulic setting and $C_i(\boldsymbol{x}, t_p)$ the corresponding salinity component at 'present state' t_p. $C_B(\boldsymbol{x}, \infty)$ is the bulk steady-state salinity induced by the superposition of all salinisation processes for the same hydraulic setting as for $C_i(\boldsymbol{x}, \infty)$ and is used to normalise the salinity differences of the respective salinisation processes.

The risk index is a measure of the stability of the system at any point, indicating how close its salinity is to steady-state conditions, but is not directly related to the absolute salinity values. A point in the domain with a 'present state' salinity close to the steady-state salinity will yield very small risk indices although this point may be highly saline. Only by confronting the risk indices with the 'present state' salinity and with a defined salinity threshold allows delimitation and identification of areas at risk.

3. Salinisation risk assessment components

As can be seen from Eq. (1), the salinity components required to obtain the risk index $R_i(\boldsymbol{x})$ of the ith salinisation process are the salinity distributions $C_i(\boldsymbol{x}, t_p)$ and $C_i(\boldsymbol{x}, \infty)$, at 'present state' t_p and at steady-state ($t = \infty$), respectively, as well as the bulk salinity distribution at steady-state $C_B(\boldsymbol{x}, \infty)$. The simulated salinity distribution $C_i(\boldsymbol{x}, t_p)$ is the salinity component of the ith salinisation process at 'present state' t_p, being the time corresponding to the measured bulk salinity distribution $C_B^*(\boldsymbol{x}, t_p)$. Assuming non-reactive solute transport as described by the classical advection dispersion equation (ADE), and, at this stage, neglecting issues related to density-driven flow and secondary salinisation processes, the salinity at any point $\boldsymbol{x}$ in a domain results from linear mixing of different fractions with different salinities. Under these conditions, the bulk salinity distribution $C_B(\boldsymbol{x}, t)$ is the sum of the n salinity components $C_i(\boldsymbol{x}, t)$ at any time t, as follows:

$$C_B(\boldsymbol{x}, t) = \sum_{i=1}^{n} C_i(\boldsymbol{x}, t) \tag{2}$$

Using the simple but useful relationship in Eq. (2) allows decomposition of a simulated bulk salinity evolution $C_B(\boldsymbol{x}, t)$ by adapting the boundary conditions accordingly.

In practice, decomposition of the salinity components according to Eq. (2) first implies calibration of a flow and transport model to fit the observed bulk salinity distribution $C_B^*(\boldsymbol{x}, t_p)$ at a given

'present state' t_p. Then, the observed bulk salinity $C_B^*(\boldsymbol{x}, t_p)$ is replaced by the simulated bulk salinity distribution $C_B(\boldsymbol{x}, t_p)$, which is used for decomposition. The salinity distribution induced by the ith salinisation process, $C_i(\boldsymbol{x}, t_p)$ is then simulated by keeping the identical flow conditions as for the calibrated simulation of $C_B(\boldsymbol{x}, t_p)$, but de-activating all transport boundary conditions apart from the one that is used to simulate the ith process.

The n salinity component pairs $C_i(\boldsymbol{x}, t_p)$ and $C_i(\boldsymbol{x}, \infty)$ are then obtained by n simulations, one for each salinisation process for the time t_p as well as for steady-state conditions ($t = \infty$), yielding the necessary components to calculate the risk index distributions $R_i(\boldsymbol{x})$ of each salinisation process by solving Eq. (1).

In summary, the pre-processing stages of the risk assessment methodology can be subdivided into two steps, shown in Table 1:

(i) Field investigations yielding the data that allow correct identification of different salinisation processes by means of hydrochemical and hydrogeological criteria.
(ii) Numerical simulation procedures, including a calibration and decomposition phase, yielding the salinity components necessary for the risk mapping procedure.

The decomposition phase is illustrated in Fig. 1 on a synthetic 2D horizontal finite element model, with two irrigation wells. In this example, two salinisation processes are superimposed in a similar way as in the real case that will be presented later in this work: irrigation salinity (IS) is superimposed on the effects of seawater intrusion.

Fig. 1a and b show the bulk salinity distributions, for the 'present state' t_p and for steady-state conditions ($t = \infty$), respectively. The seawater intrusion is simulated with a constant concentration boundary condition, while the irrigation salinisation is simulated by a mass source term on the entire domain. By adapting the boundary conditions and the source term, these two salinity distributions are decomposed into an irrigation salinity (IS) component ($i = 1$) and seawater intrusion component ($i = 2$), shown in Fig. 1c–f.

Fig. 1a shows that seawater intrusion takes place along an inflowing boundary in the north-west, whereas the regional flow takes place from the east towards south-west. Two wells are used to irrigate the entire surface, which leads to irrigation-induced groundwater salinisation due to solute recycling on the entire domain. Fig. 1c and e show the irrigation salinity components $C_1(\boldsymbol{x}, t_p)$ and $C_1(\boldsymbol{x}, \infty)$ for the 'present state' t_p and steady-state, respectively, and was obtained by imposing $C = 0$ along the inflowing boundaries and simulating the effect of irrigation-induced mass loading as mass source term (IS) on the entire domain. Fig. 1d and f show the seawater intrusion components $C_2(\boldsymbol{x}, t_p)$ and $C_2(\boldsymbol{x}, \infty)$, respectively, which resulted from simulation without the irrigation mass source term (IS = 0) on the domain, but with active lateral boundaries ($C = 1$ along shoreline and $C = 0.03$ along eastern limit).

Table 1
Schematic illustration of the pre-processing steps of the risk assessment procedure, yielding the components for the risk index definition in Eq. (1) of each of the n salinisation processes, $C_i(\boldsymbol{x}, t_p)$ as well as $C_i(\boldsymbol{x}, \infty)$ and $C_B(\boldsymbol{x}, \infty)$.

Field investigations	Numerical simulations	
Hard data	Model construction	Decomposition phase
Identification of the n existing salinisation processes (e.g. geochemical investigations)	*Elaboration of model* Definition of n transport boundary conditions (or source terms) to simulate the identified salinisation processes	Salinity components C_i $(\boldsymbol{x}, t_p)$ at time t_p ('present state'): Running one transient simulation for each of the n salinisation processes separately, by adapting the boundary conditions
Measured bulk salinity distribution C_B^* $(\boldsymbol{x}, t_p)$: 'present state' at time t_p	Calibration of model: $C_B(\boldsymbol{x}, t_p)$ Transport calibration using observed bulk salinity evolution $C_B^*(\boldsymbol{x}, t_p)$: to obtain $C_B(\boldsymbol{x}, t_p)$	Salinity components C_i $(\boldsymbol{x}, \infty)$ and C_B $(\boldsymbol{x}, \infty)$ at steady-state ($t = \infty$): Running a steady-state simulation for each of the n salinisation processes as well as for the bulk salinity distribution C_B $(\boldsymbol{x}, \infty)$

4. Risk mapping procedure

To identify areas that require remediation and conservation with respect to different salinisation processes, the risk indices have to be confronted with a threshold salinity C_T, e.g. the salt tolerance of cultivated crops in an area. The definition of such a threshold salinity C_T has to be based on criteria related to different fields, such as agronomy, irrigation science and economy and may vary in different contexts. Since definition of a threshold concentration C_T is beyond the scope of this work, we will illustrate the risk index mapping procedure, assuming that a threshold concentration has been defined. A reasonable threshold concentration could for instance be defined as the limit of exploitability for irrigation purposes or as the salinity level beyond which crop yield is drastically reduced, hence having economic implications.

The steps of the risk mapping procedure for the schematic 2D model shown in Fig. 1 are illustrated in Fig. 2, using a threshold concentration of $C_T = 0.06$, corresponding to twice the freshwater concentration (along the freshwater limit in the east) and a critical risk index value $R_C = 0.05$, implying that almost no further salinity increase is tolerated. The first step of the procedure involves projection of the defined threshold concentration C_T–iso-contour of the 'present state' salinity components $C_i(\boldsymbol{x}, t)$ onto the respective risk index distributions $R_i(\boldsymbol{x})$ (stippled lines in Fig. 2a and b), allowing subdivision of the entire domain into areas with salinities exceeding the threshold salinity ($C_i(\boldsymbol{x}, t_p) > C_T$) and areas where the salinities are below the threshold salinity ($C_i(\boldsymbol{x}, t_p) < C_T$). A similar procedure is then carried out for the risk index distributions $R_i(\boldsymbol{x})$, for which a critical index value R_C has to be chosen depending on the context, yielding areas exceeding R_C and areas where the risk indices are below R_C for each salinisation process. The entire domain can be subdivided into different risk zones, requiring different management actions. The link between the risk indices $R_i(\boldsymbol{x})$, the 'present state' salinity components $C_i(\boldsymbol{x}, t_p)$ and the management actions can then be defined according to specific criteria, shown in Table 2. As an example, the high risk areas, defined by concentrations exceeding the threshold concentration C_T require remediation in the areas where the risk indices are lower than the critical index value R_C. These are typically areas where salinisation is already advanced, approaching steady-state conditions. In the areas where the threshold concentration and the critical risk index value are exceeded, remediation and conservation are required. These areas will suffer from further salinisation if no conservation actions are taken but they are already beyond the threshold concentration C_T, therefore also requiring remediation actions. For seawater intrusion, for instance, such management actions could involve artificial recharge as remediation action and extraction control as a conservation action.

The delimitation into different risk areas can be seen to yield very different results for the two salinisation processes, i.e. the high risk areas for the seawater intrusion are located along the coast, while the high risk areas of the irrigation-induced salinity are located in the south-west.

4.1. Limitations and implications for real case situations

Although the proposed risk mapping procedure is theoretically useful, synthesising the results from dynamic processes obtained

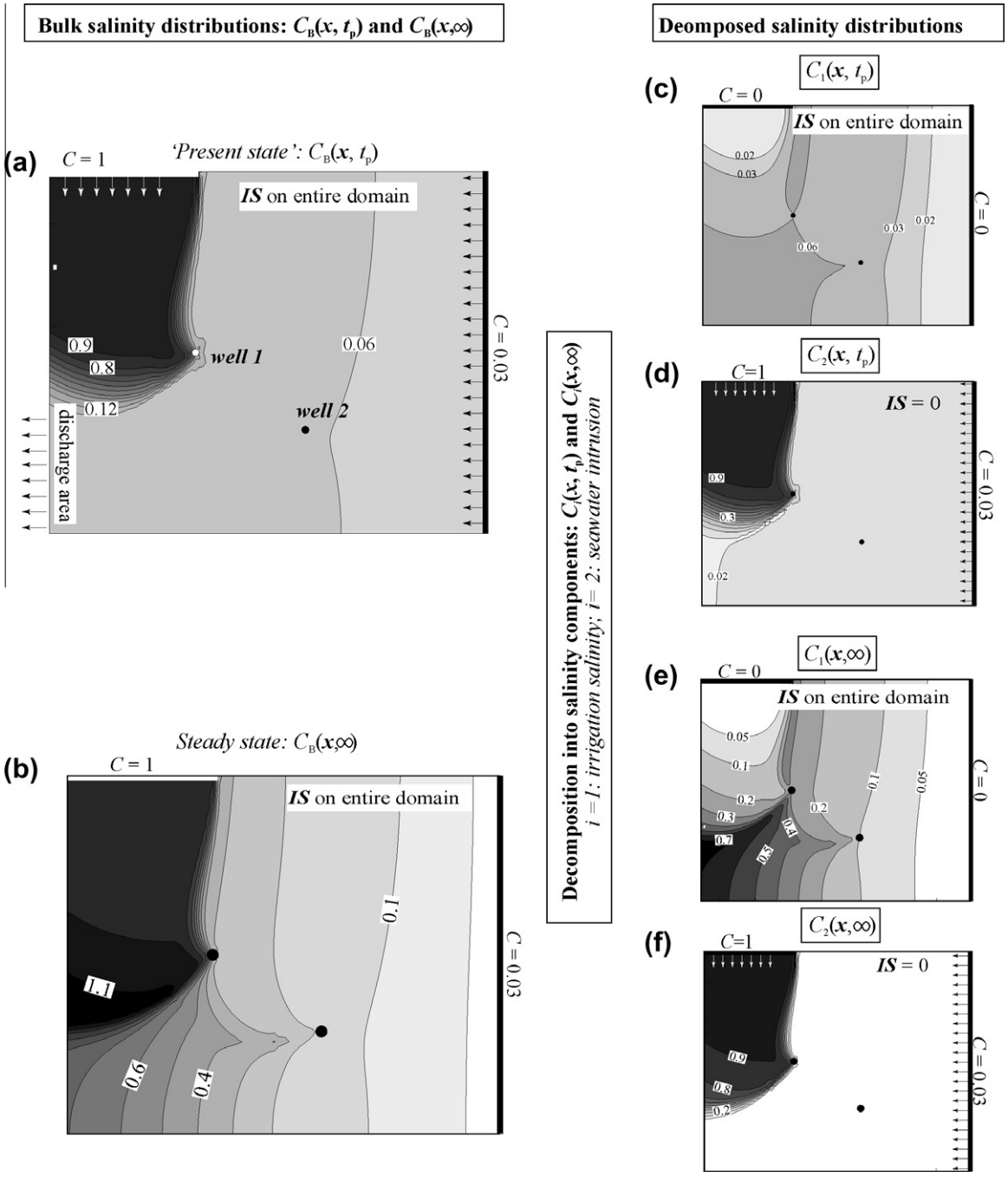

Fig. 1. Schematic illustration of the decomposition procedure on a 2D horizontal model (600 m × 350 m) with an inflowing boundary in the east and a regional discharge area in the south-west with a saline boundary in the north-west and two irrigation wells used to irrigate the entire area: (a) bulk salinity distribution $C_B(\boldsymbol{x}, t_p)$ at 'present state' t_p; (b) bulk steady-state salinity distribution $C_B(\boldsymbol{x}, \infty)$; (c) $i = 1$, 'Present state' irrigation salinity (IS) component $C_1(\boldsymbol{x}, t_p)$; (d) $i = 2$, 'Present state' seawater intrusion component $C_2(\boldsymbol{x}, t_p)$; (e) $i = 1$, steady-state irrigation salinity (IS) component $C_1(\boldsymbol{x}, \infty)$; (f) $i = 2$, steady-state seawater intrusion component $C_1(\boldsymbol{x}, \infty)$.

by numerical modelling in static images, the underlying assumption of linear superposition of the different salinisation components suffers from severe restrictions in some cases. When salinisation processes are coupled or when density-driven flow and transport is important, the basic assumption is potentially violated.

As a typical example of a salinisation-stricken aquifer, the Akrotiri aquifer which will be presented hereafter, involves several such problems, which renders direct applicability of the proposed procedure difficult. A possible way of approaching such interdependencies is to make assumptions which allow approximation of the applicability of linear superposition, as for instance evaluating whether and which dependent salinisation processes can be approximated by independent processes. In the case of entirely dependent salinisation processes, as for instance evaporative salinisation which entirely depends on solutes available in the system, use can be made of the relationship given in Eq. (2), stating that the sum of all salinity components add up to the bulk salinity component. Hence, deducing the independent salinity components from the bulk salinity components may yield an acceptable approximation of the dependent salinity component.

One aspect which additionally renders such assumptions acceptable in many cases is that the simulation results are used

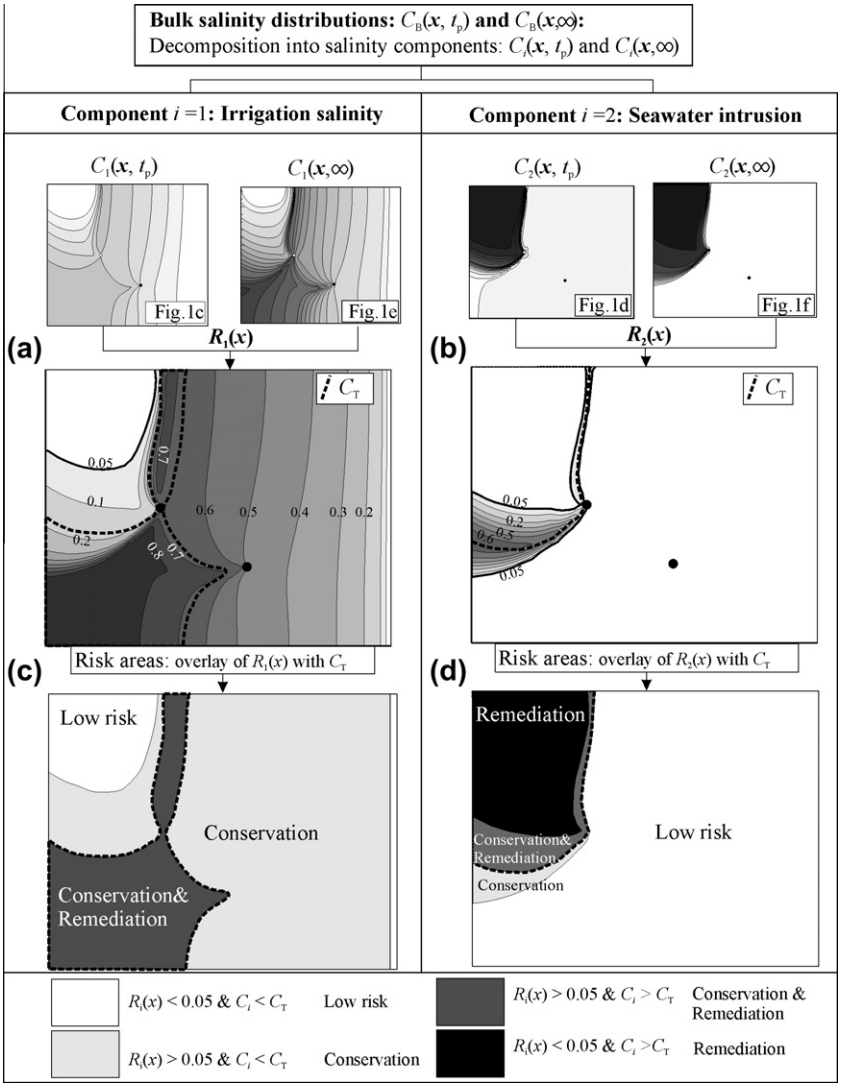

Fig. 2. Schematic illustration of the risk mapping procedure, using the same schematic model as shown in Fig. 1 for a critical risk index $R_C = 0.05$. (a) Risk index distribution for the irrigation salinity component with indicated iso-contour of the threshold salinity $C_T = 0.06$ and of the 'present state' component, (b) risk index distribution for the seawater intrusion component with indicated iso-contour of the threshold salinity $C_T = 0.06$ of the 'present state' component; (c) risk zonation with respect to irrigation salinity; (d) risk zonation with respect to seawater intrusion.

Table 2
Subdivision of the 'present state' salinity component $C_i(\boldsymbol{x}, t_p)$ into areas above and below a defined threshold salinity C_T and intersection with areas above and below a critical risk index R_C yields the respective salinisation risk areas requiring different management actions, such as conservation or remedial measures.

Salinisation risk areas	'Present state' salinity $C_i(\boldsymbol{x}, t)$ versus threshold concentration C_T	Risk index $R_i(\boldsymbol{x})$ versus critical risk index R_C	Action
High risk	$C_i(\boldsymbol{x}, t_p) > C_T$	$R_i(\boldsymbol{x}) > R_C$	Conservation and Remediation
High risk	$C_i(\boldsymbol{x}, t_p) > C_T$	$R_i(\boldsymbol{x}) < R_C$	Remediation
Intermediate-high risk	$C_i(\boldsymbol{x}, t_p) < C_T$	$R_i(\boldsymbol{x}) > R_C$	Conservation
Low risk	$C_i(\boldsymbol{x}, t_p) < C_T$	$R_i(\boldsymbol{x}) < R_C$	Conservation
Low risk: long-term amelioration	$C_i(\boldsymbol{x}, t_p) > C_T$	$R_i(\boldsymbol{x}) < 0$	Conservation
Very low risk	$C_i(\boldsymbol{x}, t_p) < C_T$	$R_i(\boldsymbol{x}) < 0$	No action required

for large-scale mapping purposes and not for any precise prediction of the solute evolution at a particular point in the domain.

5. Application to the Akrotiri aquifer (Southern Cyprus)

In this section, the described salinisation risk assessment methodology is applied and tested on a coastal irrigated aquifer system in Southern Cyprus (Akrotiri aquifer), where hydrochemical and hydrogeological investigations showed that at least three salinisation processes are superimposed (Meilhac, 2003). Groundwater salinisation is caused by seawater intrusion, irrigation-induced salinisation and by evapo(transpi)ration from the groundwater table. Hence, seawater intrusion is the only purely primary salinisation process while the other two salinisation processes depend (at least partially) on solutes already available in the system (i.e. secondary processes).

The Akrotiri aquifer has been managed in the belief that seawater intrusion is the only salinisation process. Progressive

groundwater salinisation led to an authority-controlled groundwater management scheme in the early 1990s when seawater intrusion became alarming, assigning fixed extraction rates according to the size of the plots, no matter where in the aquifer. Extraction rates were thereby controlled, leading to an amelioration of the seawater intrusion. However, groundwater salinisation in the inland areas continued, since irrigation-induced and evaporative groundwater salinisation were not considered in the management scheme.

An illustrative example from the Akrotiri aquifer, showing the possible consequences of a management scheme which is not adapted to the active salinisation process at a given location was when several hectares of orange trees died in the inland area within few weeks after an exceptionally wet winter in 2003/2004. The water table rose and led to water logging and enhanced evaporation and salt accumulation in the root zone. Although the farmers were aware that lowering the water table by increasing the extraction rates would save the trees from dying, they would have been sanctioned for doing so. The authorities did not have a management tool allowing them to decide on possible exceptions to be made.

In the following, the hydrogeological setting and the identification of the salinisation processes in the Akrotiri aquifer is first presented, followed by the description of the model construction and calibration phase, leading over to the simulation of the salinisation components and to the salinisation risk maps of the area.

5.1. Hydrogeological setting of the Akrotiri aquifer

The Akrotiri aquifer is located in the southern most part of Cyprus, in the Eastern Mediterranean, forming part of the Akrotiri peninsula (Fig. 3). It is the most important porous aquifer of Southern Cyprus with an approximate surface area of 45 km^2, consisting of deltaic deposits with thicknesses varying between 20 and 50 m (Constantinou, 1970; Jackovides, 1982; Kitching, 1975). The climatic conditions are typically semi-arid, with annual average precipitation rates of 450 mm/year and approximately 1300 mm/year of potential evaporation. Fig. 3 shows the main physiographic features of the aquifer as well as the hydrogeological conceptual model in a cross-section: recharge of the alluvial aquifer takes place by infiltration of rainfall as well as from the underlying Tertiary limestones along a major fault zone. The groundwater is extracted by irrigation wells, provoking seawater intrusion and irrigation-induced salinisation. The salt lake in the south is the hydraulically lowest point (average −2 masl) and acts as a regional discharge area, where salt precipitation and groundwater salinisation take place due to intensive evaporation.

Heavy exploitation of the aquifer started with the development of two major fruit plantations, in the late 1930s. The plantations cover an area of approximately 15 km^2 in the central part of the aquifer. Between 1940 until the 1980s an average of 14×10^6 m^3/year were extracted. Growing water demand in Cyprus led to the construction of the Kouris dam in 1986, about 10 km upstream of the Akrotiri aquifer which reduced the fresh groundwater recharge (Jackovides, 1982). This enhanced seawater intrusion which became alarming by the end of the 1980s, which led to the mentioned authority-controlled groundwater management scheme, reducing the extraction rates to approximately 8 Mm^3/year. The hydraulic depression in the aquifer, causing the landward migration of seawater, could thereby be controlled. However, seawater intrusion, groundwater salinisation induced by irrigation and direct evaporation along the inland salt lake continued, at a slower pace.

5.1.1. Water budget for different hydraulic time-periods

The hydraulic history of the Akrotiri aquifer can roughly be subdivided into three periods:

- 'Pre-1940s'-period when no extraction took place and the Kouris River still flowed
- '1940–1986'-period, when extraction was intensive and the Kouris River still flowed
- 'Post-1986'-period, when extraction was decreased but the Kouris River was dammed, no longer recharging the aquifer.

The subdivision of these three periods is based on the presence/absence of extraction wells and on the presence/absence of the Kouris River flowing through the Akrotiri aquifer area. Due to the length of the 'hydraulic periods', they can roughly be considered as hydraulic steady-state conditions with transitions of only few years between them. Each of these periods had its own water budget, which is compiled in Table 3. The water budget for the '1940–1986'-period is taken from Jackovides (1982), based on data between 1966 and 1976. The water budget for the 'Post-1986'-period was elaborated by Milnes (2000) based on data between 1987 and 1999. The imbalances shown in Table 3 in the freshwater budgets indicate the annual net water volumes which are exchanged between the aquifer system and the sea. Although the imbalance is positive for all three time-periods, there is only a surplus of 1.4 Mm^3/year for the 'Post-1986'-period, as opposed to 13.5 Mm^3/year for the '1940–1986'-period, although the extraction rates had been drastically diminished. A positive freshwater balance does not imply that there is no seawater intrusion, since it only is an overall budget (i.e. 'freshwater towards the sea' > 'seawater towards land').

The components of this freshwater budget, apart from the Kouris River which was calculated by Jackovides (1982), are briefly summarised in the following, forming the basis for definition of the boundary conditions of the numerical model simulations.

5.1.1.1. Infiltration from precipitation. The Thorntwait-Mather method (1955) was used to calculate the monthly effective infiltration. Since most of the surface sensitive to infiltration is irrigated, and therefore already humid, soil retention of only 50 mm was used, for unsaturated zone depths varying between 5 and 10 m. The obtained average value of annual infiltration is 4.9 Mm^3/year for the 'Post-1986'-period, which is coherent with the estimation of infiltration by Jackovides (1982), being 5.9 Mm^3/year for the '1940–1986'-period.

5.1.1.2. Subsurface recharge. Subsurface inflow into the Akrotiri aquifer takes place from the northern foothills, as schematically shown in the cross-section in Fig. 3. With a total surface of 100 km^2 of outcropping limestones, dipping towards the Akrotiri aquifer, the effective infiltration on this surface was estimated to be 12.3 Mm^3/year. However, to account for the higher soil retention caused by the thick unsaturated zone and for the fact that not all of the water from the limestones will recharge the Akrotiri aquifer, 70% was estimated, yielding 5.2 Mm^3/year, again coherent with the estimations done by Jackovides (1982), being 4.2 Mm^3/year for the '1940–1986'-period.

5.1.1.3. Artificial recharge. After the construction of the Kouris dam in 1986, artificial recharge has been done via infiltration ponds in the Kouris river bed, using water from the dams. The average yearly infiltration rate is 1.1 Mm^3/year for the 'Post-1986'-period.

5.1.1.4. Return flow from irrigation. Jackovides (1982) estimated that return flow from irrigation was as much as 25% for the '1940–1986'-period, but emphasised that this percentage would shortly be reduced to 10% due to improved irrigation practices. Therefore, the 10% ratio was chosen for the 'Post-1986'-period, yielding only 0.8 Mm^3/year (Table 3).

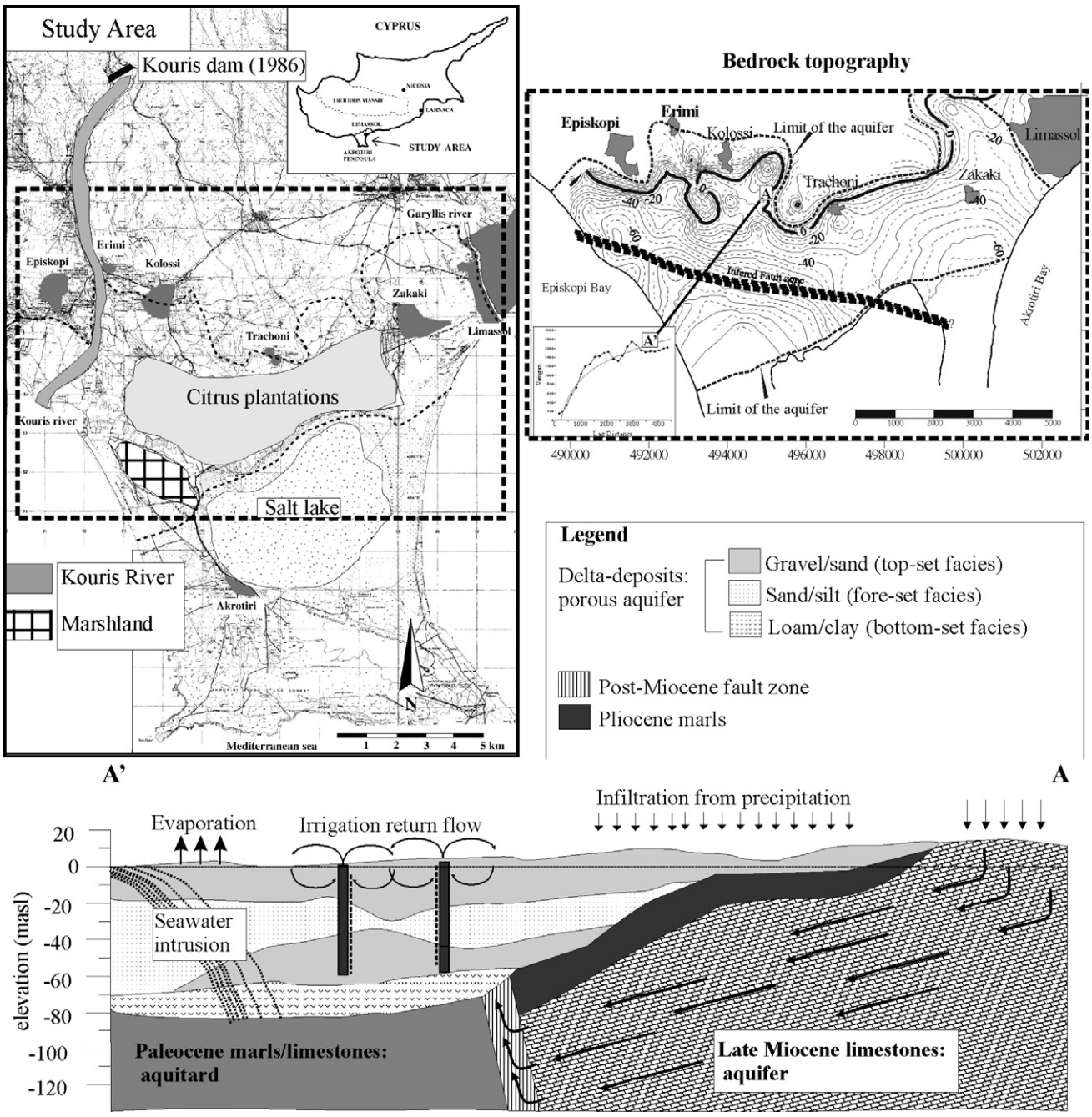

Fig. 3. Top left: General situation of the Akrotiri aquifer (stippled line), showing the shoreline to the east and to the west as well as the salt lake in the south (regional depression, −2 masl), the citrus plantations and the Kouris River and dam. Top right: Bedrock topography and large-scale fault zone. Bottom: Cross-sectional conceptual model of the Akrotiri aquifer with the three main salinisation processes.

5.1.1.5. Well extractions. The average yearly well-extraction rates for the '1940–1986'-period was 14 Mm^3/year, and continued until 1990. However, the average extraction rate in the 'Post-1986'-period is only 7.9 Mm^3/year, due to the drastic measures taken by the authorities in the beginning in 1990. Over 300 wells exist in the Akrotiri aquifer, many of them abandoned due to salinisation, and many of them only extracting very small amounts for gardens. Approximately 100 wells with high yields exist in the area, for which the extraction history and locations are known.

5.1.1.6. Evapotranspiration and evaporation from marshland. Evapotranspiration and direct evaporation take place particularly along the northern shore of the salt lake, where a vast Eucalyptus forest was planted, initially to keep the water level low during the '1940–1986'-period, when the groundwater table was too high. Also, in the south western area there is a marshland (natural depression), where evaporation is intensive. Estimated values given in literature for real evapotranspiration of aridity-resistant Eucalyptus species are 1300 mm/year (Marshall et al., 1997), corresponding to the average annual ETP evaluated by the Meteorological Department. This yields, an average of 2.6 Mm^3/year of evaporated water from the system, coherent with the estimation of Jackovides (1982), being 2.5 Mm^3/year.

5.1.2. Water level evolution

The water levels for the 'Pre-1940s'-period are not known, however, since no extraction took place, it can be assumed that

Table 3
Long-term annual average values for the freshwater balance for the three defined hydraulic periods: values are given in Mm^3/year. Values for the '1940–1986'-period are taken from Jackovides (1982). Since the water balance for the 'Pre-1940'-period is not known, the same values were used as for the '1940–1986'-period (indicated with stars). The difference between the two periods lies in the lack of extraction rates prior to 1940. The water budget for the 'Post-1986'-period was established in Milnes (2000). The calculated imbalances indicate the net exchange between the sea (and salt lake) and the aquifer.

Water budget component	'Pre-1940s'-period (Mm^3/year)	'1940–1986'-period (Mm^3/year) (Jackovides, 1982)	'Post-1986'-period (Mm^3/year) (Milnes, 2000)
Kouris river infiltration	15.4*	15.4	–
Infiltration from precipitation	5.9*	5.9	4.9
Subsurface recharge	4.2*	4.2	5.1
Artificial recharge	–	–	1.1
Return flow from irrigation	–	4.5	0.8
Evaporation (eucalyptus forest and marshlands)	−2.5*	−2.5	−2.6
Well extractions	–	−14.0	−7.9
Imbalance	+23.0	+13.5	+1.4

* Assumed equal to the '1940–1986'-period

the system was in equilibrium with steady-state hydraulic conditions, apart from seasonal variations.

For the time-period between '1940 and 1986', water levels were mostly above sea level, with a significant amount draining towards the salt lake (Jackovides, 1982).

During the 'Post-1986'-period, the water levels were lowered below sea level in many places. During the first few years after the construction of the Kouris dam in 1986, until 1990, the water level decline was prominent, but then rapidly stabilised on the lower level, as soon as the extraction rates were diminished. The water level evolutions for four selected observation wells, two of which have been measured since 1964, are shown in the graph in Fig. 4. A prominent water level decrease was observed in the early 1970s during the '1940–1986'-period, which was due to an exceptional drought period (Jackovides, 1982). The water level decline between 1986 and 1990 is nicely revealed, as well as the stabilisation after 1990. Over a long-term period, the analysis of the water level evolutions of all observation wells revealed, that the 'Post-1986' hydraulic situation can be approximated by steady-state conditions on the long-term. The average water level distribution for the 'Post-1986'-period is shown in Fig. 4 and is based on monthly data taken in 120 boreholes. The water levels can be seen to be negative in the entire central area. The prominent groundwater depression in the area of the salt lake is nicely revealed, leading to converging flow paths.

5.1.3. Salinisation processes in the Akrotiri aquifer

The electrical conductivity distribution measured in 70 observation wells in the superficial groundwater in summer 2003 is shown in Fig. 5, resulting from all salinisation processes present in the system. This salinity distribution corresponds to the measured bulk salinity distribution $C_B^*(\boldsymbol{x}, t_p)$, defined in the risk mapping procedure.

To distinguish between different salinisation processes, a large-scale hydrochemical investigation was carried out in the Akrotiri aquifer in July 2003 (Meilhac, 2003), with the main results and data presented in Milnes et al. (2006). Geochemical markers combined with hydrogeological criteria were used to identify the different salinisation processes, allowing subdivision into a seawater intrusion and an irrigation/agriculturally dominated domain, respectively, and an area dominated by evaporative salinisation in the vicinity of the salt lake. The spatial distribution of the salinisation processes is schematically shown on the bottom left of Fig. 5.

The criteria used for the identification of the processes can be summarised as follows:

Seawater intrusion

- Presence of a sharp seawater–freshwater interface, measured in vertical conductivity logs.
- Major ion ratios indicating simple mixing and cation exchange.
- Stable as well as radioactive isotope signatures (with distinct uranium isotopic ratios of seawater to track mixing processes) indicating mixing between fresh groundwater and the seawater end-member (Milnes, 2005).

Irrigation and agriculturally induced salinisation

- Intermediate salinities of 1.5–5 mS/cm.
- High nitrate concentrations (up to 400 mg/l).
- Uranium isotopic signatures close to the freshwater end-member, strongly deviating from the mixing-line between freshwater and seawater, indicating evaporative processes related to irrigation (Milnes, 2005).

Salinisation induced by evapo(transpi)ration

- $\delta^{18}O$-enrichment.
- Water table close to the surface at a depth of less than 3 m.
- High salinities, sometimes close to the limit of solubility.
- Salt precipitation on the soil surface.
- Nitrate concentrations lower than in the agriculturally salinised areas.
- Prominent diurnal water table fluctuations measured in the area of the Eucalyptus forest along the salt lake indicating strong evapotranspiration (Milnes et al., 2006).

5.2. Numerical model construction and calibration

In this section, the conceptual hydrogeological model described above is transcribed into a numerical model, using the water balance and the identified salinisation processes to define boundary conditions. A 3D finite element model was constructed with the FEFLOW finite element software (Diersch, 2007). First, the model construction is described, followed by the hydraulic steady-state calibration, yielding the hydraulic parameter distribution. In a second step, the transport calibration is presented, which involved density-dependent flow and transport simulations in an iterative process for the main calibration parameter, the porosity distribution. The actual transport calibration was done for the time-period 1986–2003, for which a relevant data set exists. However, a major difficulty involved simulation of the initial concentration distribution in 1986, the starting phase for the calibration.

Density-dependent flow and transport simulations involve transient hydraulic conditions. The transitions between the different hydraulic periods were therefore actually simulated in hydraulic transient state, allowing the system to adapt to the new hydraulic conditions of the following period, using the storage coefficient distribution which had been calibrated on a 1-year period (1997–1998), described in Milnes (2000).

5.2.1. Model delimitation and internal geometry

The lateral extend of the finite element model towards the inland (north) was defined by the presence of groundwater in the

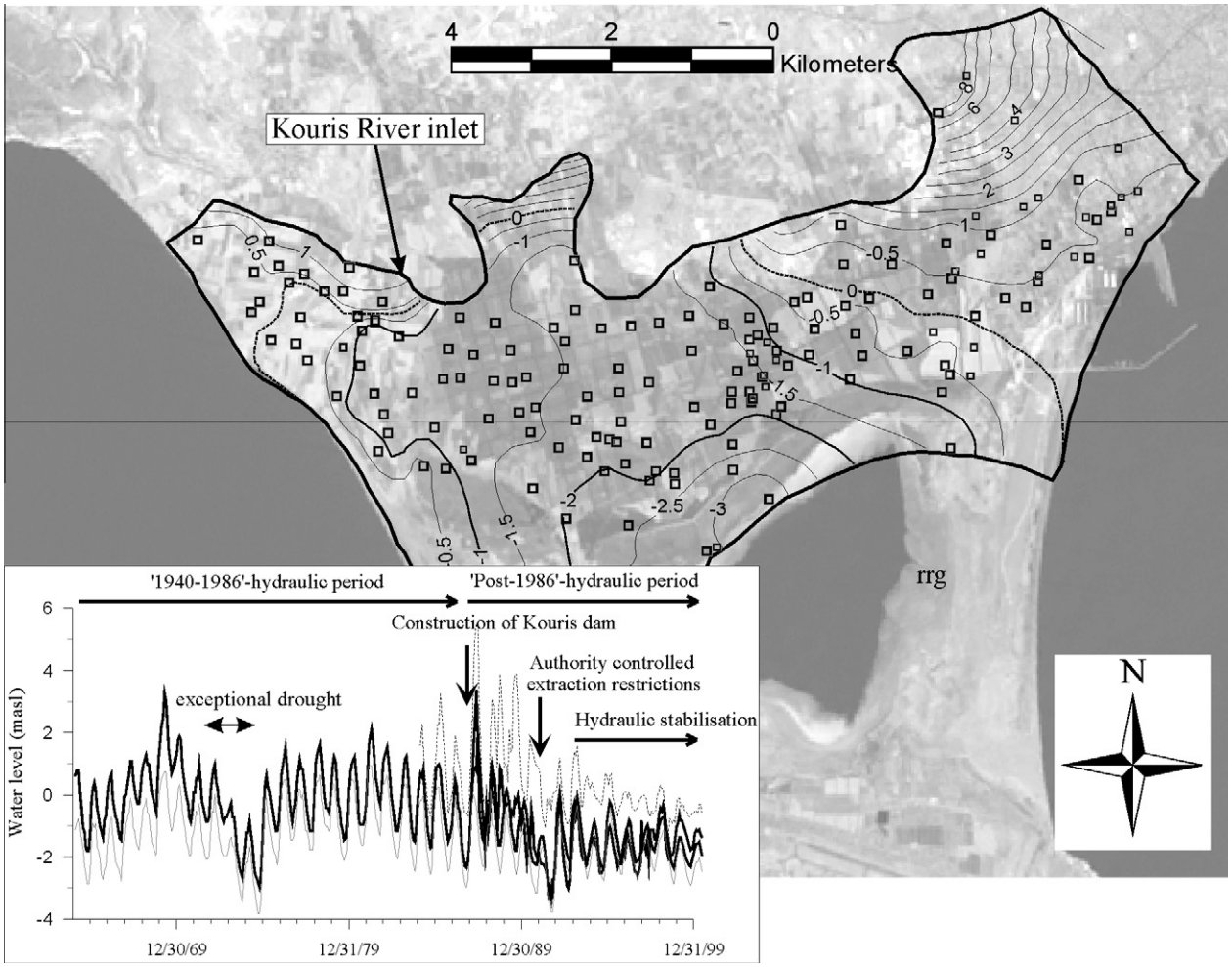

Fig. 4. Average water level distribution for the time-period 1986–2003. Observation wells are shown as squares. Bottom left: Graph showing the temporal water level evolution for four observation wells, two of them with data back to 1964. The two hydraulic periods are indicated and the time when the Kouris dam was constructed (1986) is indicated with an arrow.

gravel deposits (porous aquifer). In the east and the west, the model was extended offshore to a bathymetric depth of −50 masl, approximately corresponding to the average thickness of the porous aquifer. In the south, the model limit was drawn along the shore of the salt lake.

The internal model geometry was deduced from approx. 200 borelog interpretations (Milnes, 2000), using a simple sedimentary facies model, describing the coarsening upward cycle of the depositional sequences of delta-fan environments (Reading, 1986). The lithofacies encountered in the borelogs were assigned to one of the three classical delta facies, which are characterised by different hydraulic properties: (a) the bottom-set facies consisting of fine-grained deposits (silt, loam and clay), overlain by (b) the fore-set facies, consisting of medium-grained deposits (sand and silt) and finally (c) the top-set facies with the coarsest-grained deposits (gravel and sand). From the borelog record, the respective facies thicknesses were lumped together, which led to a 3D distribution of the superimposed facies. The three units that were constructed in this way reflect the absolute thicknesses of the respective facies but not any internal heterogeneity arising from inter-fingering (Fig. 6).

Twelve pumping tests carried out within the framework of the Akrotiri Irrigation Project 1970 (Jackovides, 1970) could be attributed to the top-set facies (gravel unit) and the fore-set facies (sand unit), respectively, yielding a range for the hydraulic conductivities: top-set facies: $K = 2 \times 10^{-3}$–5×10^{-4} m/s; fore-set facies: $K = 5 \times 10^{-5}$–1×10^{-4} m/s. The upper limits of these ranges were used as initial values for the hydraulic calibration.

The Pliocene fractured marl deposits, the Miocene limestone unit and the regional fault zone with a vertical displacement of several 100 m, as deduced from borehole data (Milnes, 2000), were incorporated in the model to accommodate the recharge that had been estimated to transit through the underlying limestones from the northern foothills, recharging the porous aquifer from below (Fig. 3). Recharge along the fault zone was identified by a prominent radon and oxygen isotopic anomaly in the groundwater above the fault zone (Meilhac, 2003).

Fig. 6 shows the subdivision of the 3D model into the six identified hydrostratigraphic units, which were used to calibrate the hydrodynamic model parameters.

5.2.2. Model discretisation

The finite element model was discretised into 170,270 linear, triangular prismatic elements, (96,030 nodes), with an average lateral extension of 100–150 m (Fig. 7), and was vertically subdivided into 11 slices. The mesh was refined around all extraction wells. A topmost layer was introduced into the model with a constant thickness of 1 m, to allow assignment of surface source terms for infiltration and solute mass loading. The mesh discretisation is a limiting factor with respect to transport simulations, since the

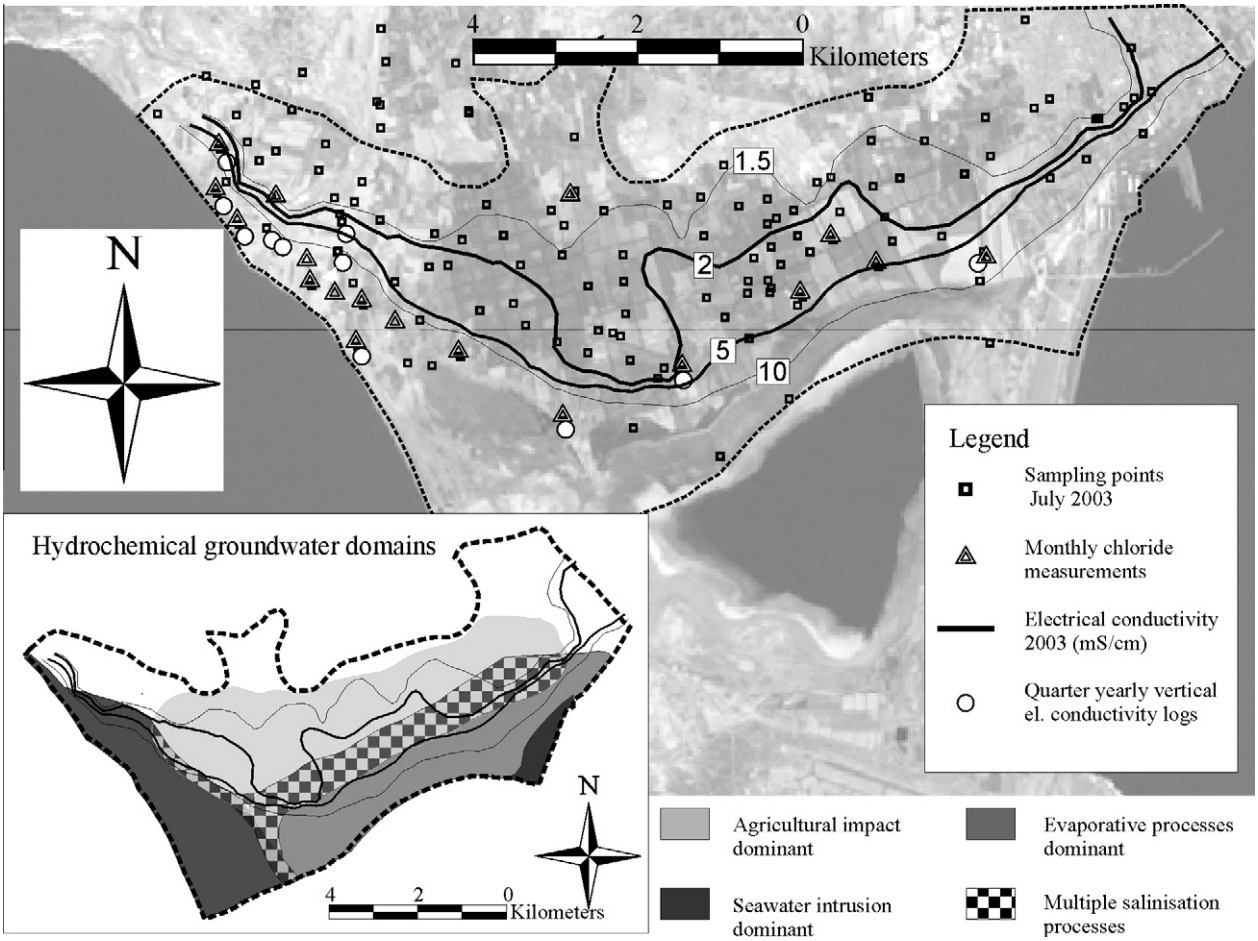

Fig. 5. Distribution of electrical conductivity (mS/cm) as measured in 70 observation wells in July 2003. Bottom left: Map showing the spatial distribution of dominant salinisation sources, resulting from hydrochemical investigations (modified after Meilhac (2003)). The chequered area indicates the areas where more than one salinisation processes are Superimposed (seawater intrusion, agricultural salinisation and evaporative processes).

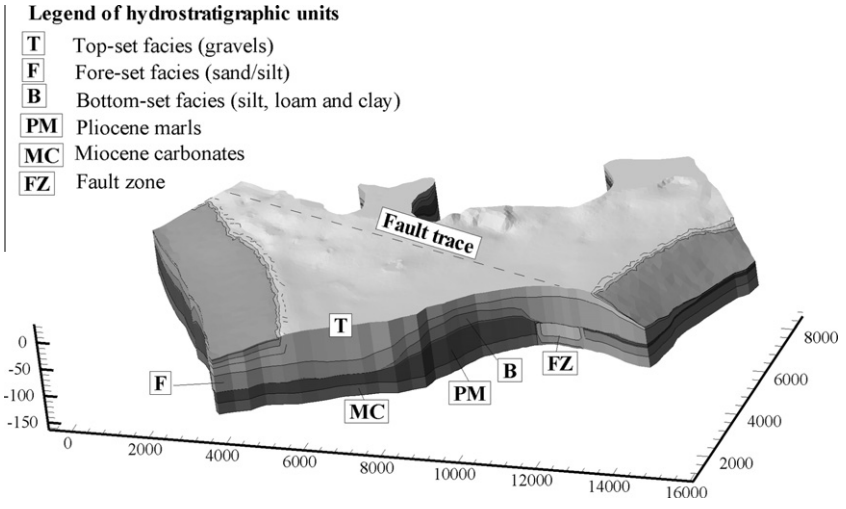

Fig. 6. 3-D view of the Akrotiri aquifer model showing the subdivision into six hydrostratigraphic units. The trace of the large-scale fault zone cutting through the Miocene carbonates and Pliocene marls is indicated on the surface. Vertical exaggeration 1:15.

dispersivity values will have to be adapted to be close to the element size, to avoid numerical instabilities. Since real dispersivity values are usually far smaller than the mesh size of regional models, this is why dispersivities can often not be calibrated in regional modelling approaches to match physical values. Hence, in the case of the Akrotiri aquifer model, the longitudinal dispersivity was fixed as $\alpha_L = 130$ m, corresponding to the average element size and a transversal dispersivity of $\alpha_T = 10$ m was assigned.

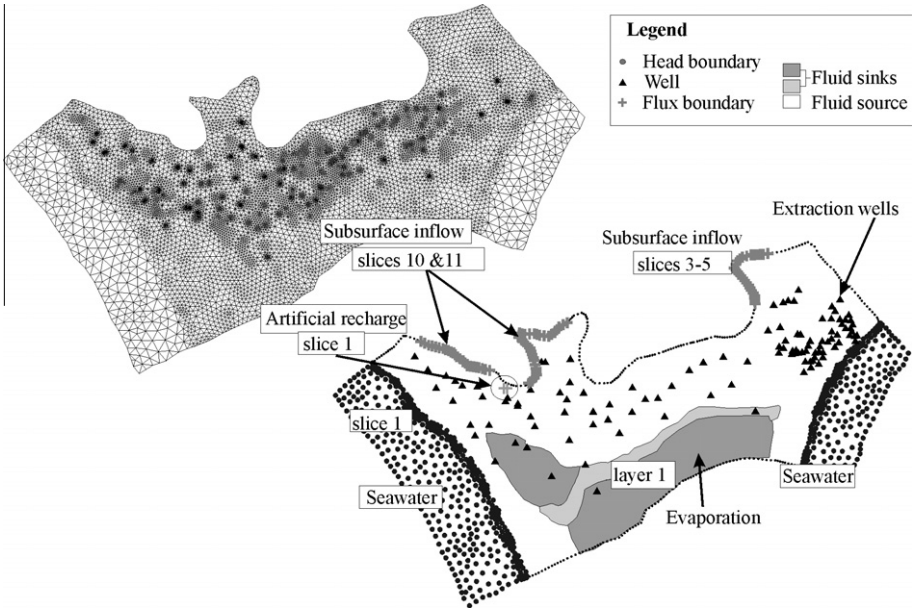

Fig. 7. Finite element mesh (top left) and hydraulic boundary conditions (bottom right) used during the hydraulic calibration phase.

5.2.3. Hydraulic steady-state calibration for the time-period 1986–2003

Hydraulic calibration was carried out on the basis of the average hydraulic condition between 1986 and 2003. One hundred and twenty observation points were used, for which monthly values were available (Fig. 4). As mentioned, this period was chosen because 1986 brought a prominent change in the hydraulic setting, with the construction of the Kouris dam.

The boundary conditions were defined to comply with the water budget presented in Table 3 , illustrated in Fig. 7 and summarised below.

5.2.3.1. Head boundary conditions. Constant hydrostatic head boundary conditions, accounting for the density difference between seawater and freshwater, were assigned on the seafloor (on the 1st slice only), according to the bathymetric depth of each node (Fig. 7).

5.2.3.2. Well boundary conditions. Well-type boundary conditions were used for the extraction wells. The well extractions were distributed throughout the depth of the gravel unit. The extraction rates were deduced from the average extraction rates from 1986 to 2003, based on monthly readings of the water meters. For insignificant wells (small extraction rates), the extraction rates were added to the closest defined significant extraction well, within a radius of 300 m, to avoid definition of hundreds of additional wells, for which the mesh would also have had to be refined. The total extraction rate was 7.9 Mm^3/year, corresponding to the water budget shown in Table 3.

5.2.3.3. Subsurface recharge. Inflowing flux boundary conditions were assigned along the northern boundary in the limestone unit (lower layers, Fig. 7) and were adjusted to match the estimated subsurface influx shown in the water budget in Table 3, corresponding to 70% of the average net infiltration on the northern limestone foothills.

5.2.3.4. Fluid sources. Recharge from rainfall was introduced into the model as a fluid source in the top layer, corresponding to 120 mm/year/m^2, and was based on the Thorntwaite and Mather (1955) method, as described in Section 5.1.1.

In the irrigated areas, irrigation return flow was added to the recharge from rainfall, with an infiltration rate corresponding to 10% of the annual irrigation rate, as described in Table 2.

Artificial recharge was introduced in the model as a flux boundary condition at the inlet of the Kouris River bed (Fig. 7), corresponding to 1.1 Mm^3/year, as described in the water balance in Table 2.

5.2.3.5. Fluid sinks. In the area of the marshland in the west and in the area along the salt lake, where evaporation is dominant, a fluid sink was defined (Fig. 7), corresponding to the net difference between the average rainfall and the pan evaporation, assigned in the top layer.

5.2.3.6. Hydraulic calibration results. Using the above-described hydraulic boundary conditions, calibration of the hydraulic conductivities of each hydrostratigraphic unit (Fig. 6) was carried out by trial and error, and in the last stage, the hydraulic conductivities and infiltration rates were fine-tuned by running simulations with an optimisation-algorithm included as a module in FEFLOW (PEST, John Doherty, Watermark Computing). The obtained calibrated hydraulic conductivities are shown in Table 4. Fig. 8a shows the measured average water table map, as well as the locations of the observation wells. Fig. 8b shows the simulated hydraulic head distribution in the gravel unit. The graphs on the left-hand side of Fig. 8 shows the correlation between the measured and simulated average hydraulic heads between 1986 and 2003, with a standard deviation of 0.2 m. The calibrated hydraulic condition reflects the main features of the average hydraulic situation, being the prominent depression induced by the salt lake, forming the regional discharge area. The smaller-scale hydraulic pattern is relatively well reproduced, although it is smoothened with respect to the measured head distribution. The calibrated hydraulic conductivity distribution, as shown in Table 4, was used for all further simulations.

5.2.4. Transport calibration of measured bulk salinity $C_B^*(\boldsymbol{x}, t_p)$

The transport calibration was also carried out for the time-span between 1986 and 2003, since the data set for this time-span is solid.

Table 4
Calibrated hydraulic conductivities and porosities of the six hydrostratigraphic units, shown in Fig. 6. The fore-set facies was subdivided into two layers (one for the sand and the second layer for the silts), yielding two values. Also two values are given for the Miocene limestones: (1) for the area north of the fault zone and (2) for the area south of the fault zone.

Hydrostratigraphic unit	Hydraulic conductivity (m/s)	Porosity (–)
Gravels (top-set facies)	4.0×10^{-4}	0.3
Sand and silt (fore-set facies): 2 layers	(1) 1.0×10^{-4}	(1) 0.2
	(2) 1.0×10^{-5}	(2) 0.2
Silt, loam and clay (bottom-set facies)	1.0×10^{-6}	0.15
Pliocene marls (fractured)	1.0×10^{-7}	0.1
Miocene limestones (fractured, slightly karstified)	(1) 1.0×10^{-4}	(1) 0.15
	(2) 1.0×10^{-5}	(2) 0.15
Fault zone	5.0×10^{-4}	0.15

All transport simulations were carried out accounting for density-dependent flow and transport induced by salinity differences between fresh groundwater and saline groundwater. The only transport parameter that was calibrated was the porosity distribution. The second calibration variable was the solute mass loading from irrigation. Since the salt loading due to irrigation partially depends on agrochemical additives, but also on the salinity of the extracted groundwater, it is not constant over the entire domain. Irrigation-induced salinisation was only considered for the time-period after 1986, since groundwater salinities in the inland area prior to the Kouris dam construction were very low.

5.2.4.1. Simulation of the initial concentration distribution. The first step in the transport calibration involved simulation of the initial concentration distribution in 1986. For this purpose, simulation of the two hydraulic periods preceding 1986 had to be simulated for each guess of porosity distribution:

- Density-dependent simulation of the situation in 1940, assuming that the system was in complete equilibrium with respect to the seawater wedge. This was obtained from a long-term simulation until stabilisation of all concentrations was attained, defining the hydraulic boundary conditions shown in Fig. 9a, based on the water budget presented in Table 2.
- The concentration distribution from the first step was used as initial concentration distribution for a density-dependent simulation of the '1940–1986'-period, with the hydraulic and transport boundary conditions shown in Fig. 9b. Since the exact location of the extraction wells for this time-period are not known, the same positions were used as for the time-period 1986–2003, however doubling all the extraction rates to comply with the water balance (Table 3).

For both simulation steps, the hydraulic boundary condition assigned to simulate Kouris River infiltration was a constant head

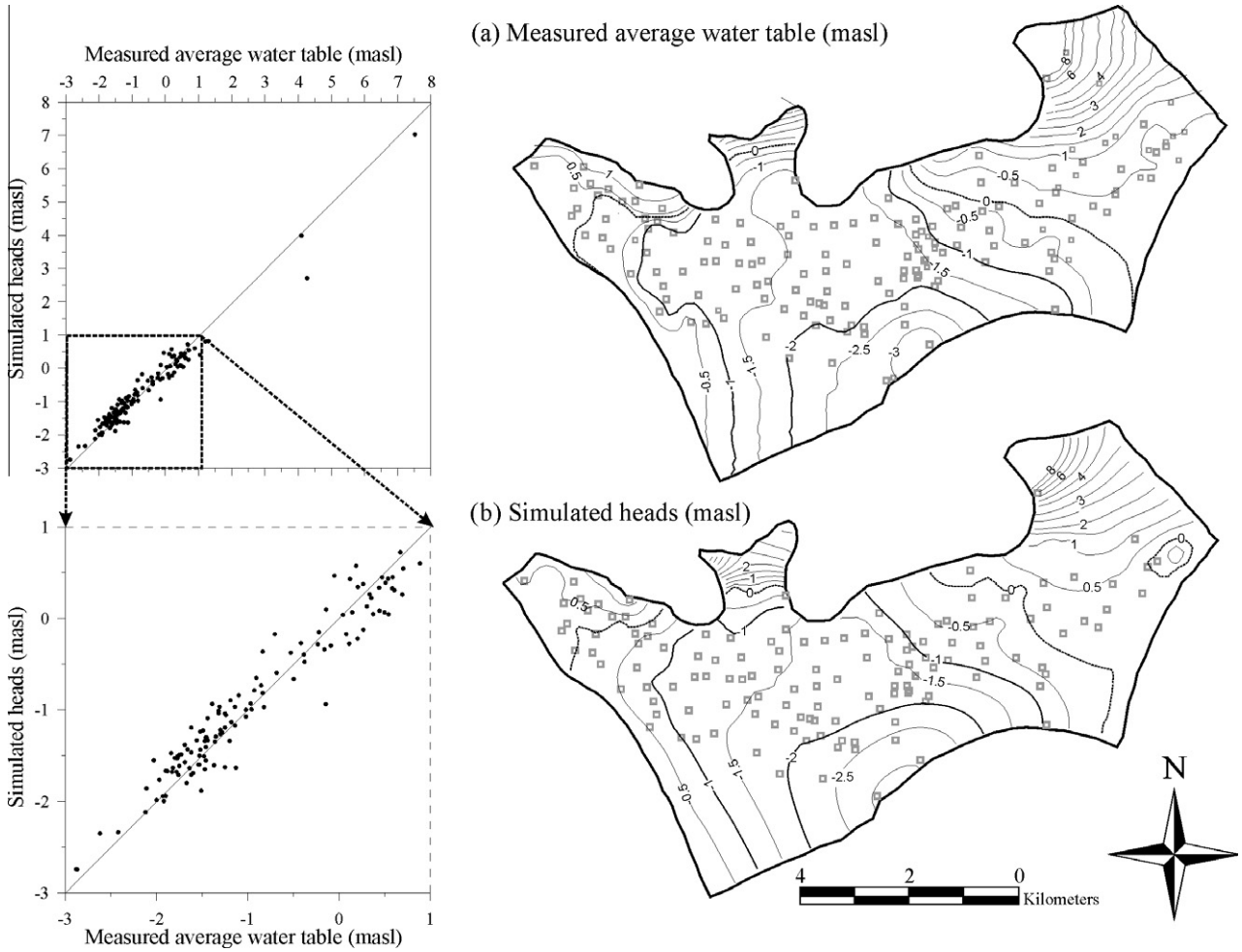

Fig. 8. Hydraulic calibration of the average water table (masl) between 1986 and 2003. (a) Measured average water table; (b) Simulated heads in the gravel layer. Left: Correlation between measured and simulated heads (bottom graph is a close-up).

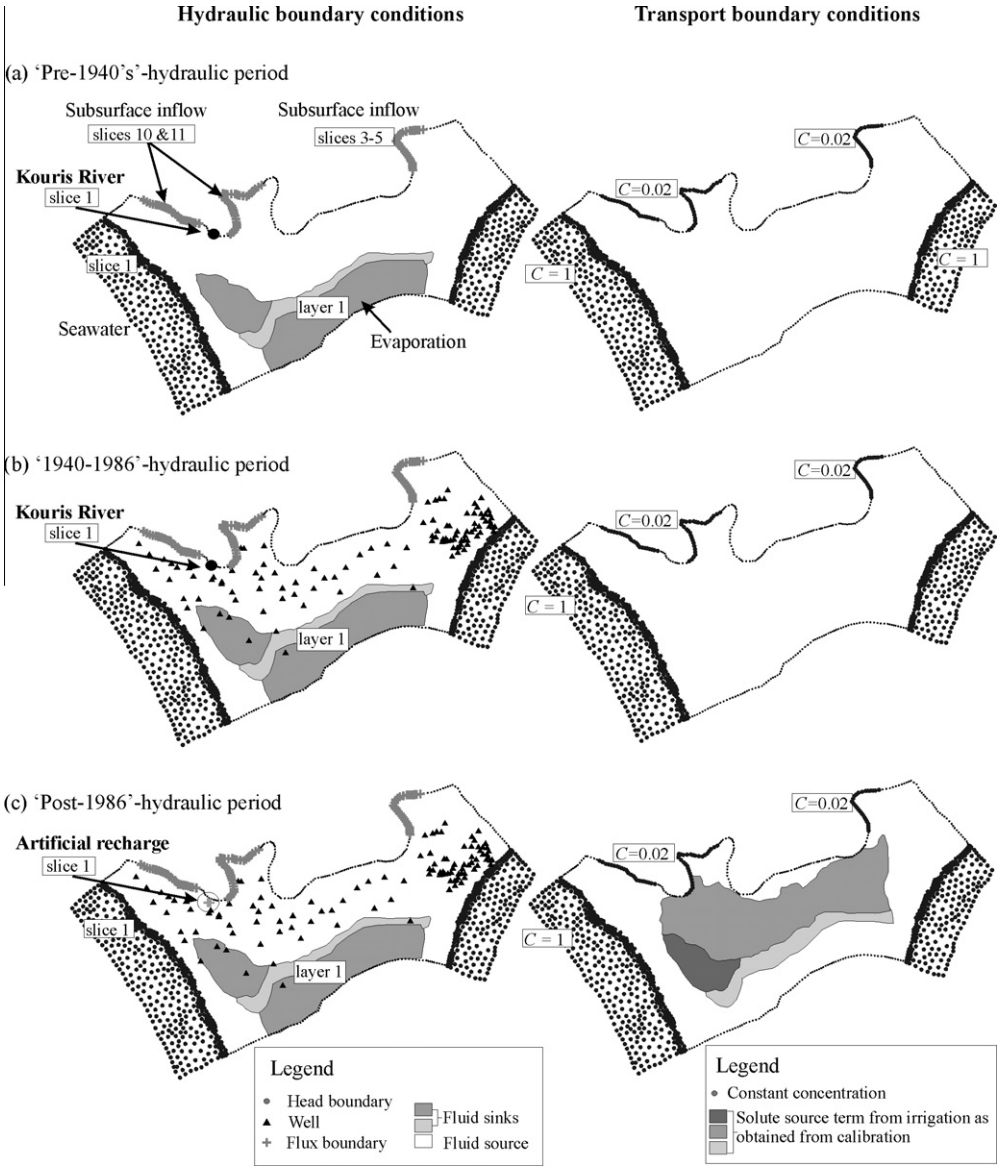

Fig. 9. Hydraulic (left column) and transport (right column) boundary conditions defined for three hydraulic periods: (a) the 'Pre-1040s'-hydraulic period, when no extraction took place but the Kouris river was flowing, (b) The '1040–1986'-period, when extraction rates were high and the Kouris River was flowing and c) the 'Post-1986'-period, when extractions were diminished and the Kouris River was dammed.

boundary at the entry of the system in the river bed, with its surface elevation as value (H = 35 m). This led to a water budget of 13 Mm^3/year, coherent with the estimations done by Jackovides (1982), shown in Table 2.

The resulting concentration distribution of these two simulation steps was first compared to the scarce salinity data set from 1986 and then used as initial concentration distribution to carry out the transport calibration for the time-period 1986–2003 for a given porosity distribution guess with the boundary conditions as shown in Fig. 9c. This led to an iterative and long process, since each porosity distribution guess required re-simulation of the initial concentration distribution for the calibration period. During the calibration phase of the '1986–2003'-period, the observation wells close to the shoreline were first used, with the densest monitoring network and the highest salinity variations. Then, in a second stage the irrigation salinity was added to calibrate the irrigation salinisation distribution.

The transport boundary conditions and source terms as well as the associated hydraulic boundary conditions assigned during each hydraulic period are shown in Fig. 9 and can be subdivided into freshwater boundaries, and salinisation boundaries.

The freshwater boundaries were simulated as follows.

5.2.4.2. Infiltration from precipitation. Since infiltration from precipitation is modelled by a hydraulic source term, the effect of this input leads to dilution in the transport equation of the solutes present in the elements, calculating the dilution with an infiltration concentration of C = 0.

5.2.4.3. Subsurface freshwater inflow. Along the inland boundaries a constant relative concentration of C = 0.02 was assigned. This value is based on the ratio between the freshwater and seawater electrical conductivities (0.02 = 1 mS/cm: 50 mS/cm). This boundary condition remained unchanged for all three simulation periods.

5.2.4.4. Kouris River infiltration. The Kouris River infiltration was only simulated for the first two hydraulic periods, prior to 1986, and implied definition of a constant concentration boundary

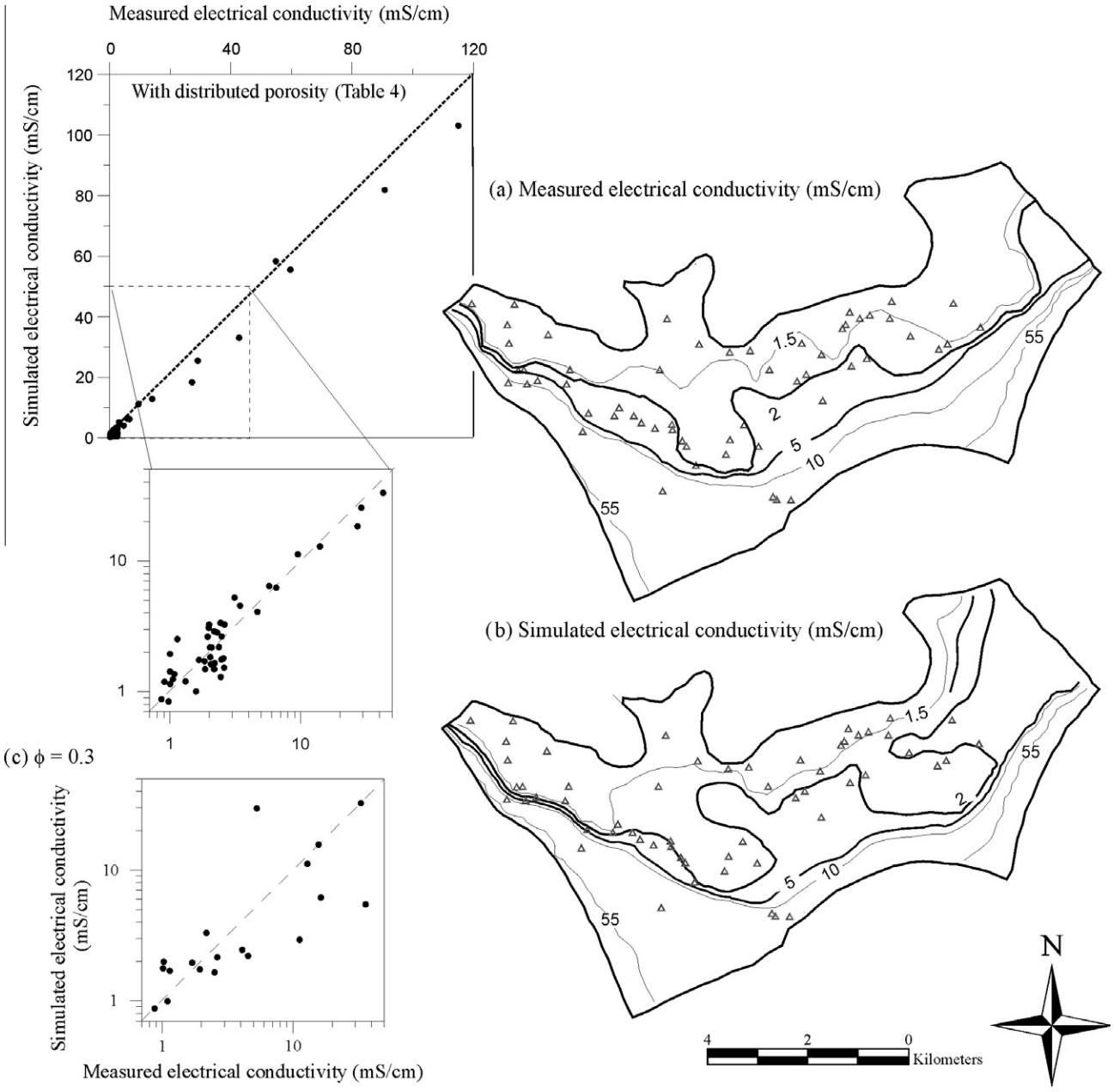

Fig. 10. Transport calibration, resulting from a distributed porosity distribution according to the lithofacies (Table 4): (a) Measured bulk salinity distribution $C_B^*(\boldsymbol{x}, t_p)$ in mS/cm; (b) Simulated bulk 'present state' salinity distribution $C_B(\boldsymbol{x}, t_p)$, transformed in terms of electrical conductivity values (mS/cm) according to Eq. (4). Left: Scatter plot of the observed versus the simulated salinities in 2003. (c) Correlation graph resulting from the initial homogeneous porosity distribution ($\varphi = 0.3$), showing a bad correlation between measured and simulated salinities.

condition on the nodes where the hydraulic head boundary conditions was defined, at the Kouris River inlet, with a constant concentration values of $C = 0.02$ (Fig. 9a and b).

5.2.4.5. Artificial recharge. For the hydraulic period 1986–2003, a constant concentration of $C = 0.02$ was assigned on the defined hydraulic flux boundary conditions at the inlet of the Kouris River (Fig. 9c), where the infiltration ponds are located, mimicking artificial recharge with an average annual infiltration rate of 1.1 Mm^3/year, as per Table 3.

The three salinisation processes, described in Section 5.1.3. were simulated by the following transport boundary conditions and solute source terms, respectively, as follows (Fig. 9).

5.2.4.6. Seawater intrusion. Seawater intrusion was simulated by the constant concentration boundary condition on the seafloor (first slice), with a relative concentration of $C = 1$. The concentration boundary condition is constrained to inflowing fluxes, i.e. in areas where groundwater discharges to the sea the concentration boundary condition is not active. This boundary condition remained unchanged for all three simulation periods.

5.2.4.7. Irrigation salinity. Distributed irrigation salinisation was adjusted during the calibration process, starting off with a spatially constant relative mass source terms on the irrigated fields, assuming an average yearly mass loading of 20 t/ha, which roughly corresponds to an absolute irrigation water salinity of 2 g/l. Solute mass loading from irrigation was only simulated for the

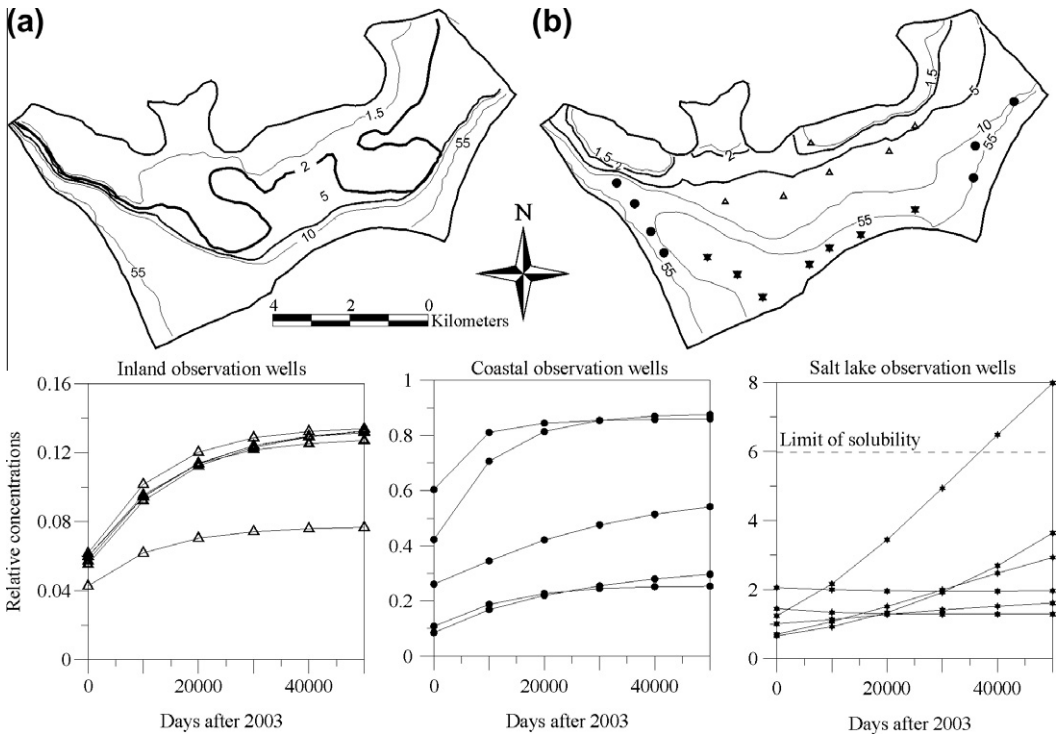

Fig. 11. Simulated bulk salinity distributions: (a) 'present state' $C_B(\boldsymbol{x}, t_p)$ and (b) 'quasi'-steady-state $C_B(\boldsymbol{x}, \infty)$, obtained from transient density-dependent simulation over a time-period of 50,000 days. The graphs on the bottom show the concentration evolution for chosen points in the domain, as indicated in (b), and reveal stabilisation of the concentrations along the shoreline and in the inland area. Concentrations along the salt lake increase steadily, even above the limit of solubility (shown as stippled line).

'Post-1986'-period, assuming that irrigation salinisation was insignificant in the previous period, due to very low groundwater salinities. Calibration of this salinisation process was done on data from the inland area, where no other salinisation process is active. This led to a spatially distributed mass source term, as shown in Fig. 9c.

5.2.4.8. Evaporative salinisation. A fluid sink was used to simulate the evaporative losses, removing only the water from the defined model elements, not however the solutes which are contained in the element. This leads to concentration (the opposite effect from dilution), mimicking salinisation by evaporation. The disadvantage of simulation of salt accumulation by a fluid sink is that concentrations will never stop to increase, tending towards infinity, since precipitation of minerals cannot be simulated, hence never reaching steady-state conditions.

5.2.4.9. Transport calibration results. Carrying out the transport simulations, as described above, the simulated concentrations were compared to the measured salinity distribution for each porosity distribution guess and was then optimised step-by-step. The resulting porosity distribution accounted for the different hydrostratigraphic units, and yielded a downward porosity decrease, with the highest porosities in the gravel unit ($\varphi = 0.3$), a porosity of $\varphi = 0.2$ in the sand/silts unit, $\varphi = 0.15$ in the silt/loams and fractured limestones and fault zone, and the lowest porosity of $\varphi = 0.1$ in the Pliocene fractured marls, as indicated in Table 4.

Since the transport simulations were carried out with relative concentrations, defining the seawater concentration as $C = 1$, an experimentally established relationship between the electrical conductivity and (the conservative) chloride concentrations was used to convert the simulated relative concentrations into electrical conductivities, allowing subsequent comparison with the measured electrical conductivity distribution. Based on 37 groundwater samples from the Akrotiri aquifer and a seawater sample, the following relationship between the chloride concentration and the electrical conductivity was established (Milnes, 2000):

$$C_{cl} = 0.422EC \tag{3}$$

with C_{cl} being the measured chloride concentration in [ppm] and EC the electrical conductivity [μS/cm], with a correlation coefficient of $R^2 = 0.994$ (Milnes, 2000). The seawater chloride concentration was $C_{sea} = 20{,}724$ ppm with a corresponding electrical conductivity of 50,300 μS/cm. The transformation of the simulated relative concentrations $C_{cl\text{-simulated}}$ into simulated electrical conductivities $EC_{simulated}$ was done making use of Eq. (3), as follows:

$$EC_{simulated} = \frac{C_{cl-simulated} \times C_{sea}}{0.422} \tag{4}$$

The result of the transport calibration is shown in Fig. 10b, reflecting the salinity distribution within the gravel aquifer unit after conversion of the simulated relative concentrations in terms of electrical conductivity, according to Eq. (4). Fig. 10a shows the salinity distribution as measured in the superficial groundwater in 2003. The graph on the left-hand side shows the correlation between the measured and simulated electrical conductivity. Fig. 10c shows the correlation between measured and simulated salinities for the initial homogeneous porosity distribution of $\varphi = 0.3$, showing that calibration of the porosity distribution is of high importance. The simulated salinity distribution shown in Fig. 10b corresponds to bulk salinity distribution at present state $C_B(\boldsymbol{x}, t_p)$, required for the risk assessment methodology. Although the described calibration procedure is long, it does not differ from any standard numerical simulation approach. This implies that the difficulty is basically inherent to numerical simulation and not related to the risk assessment methodology as such.

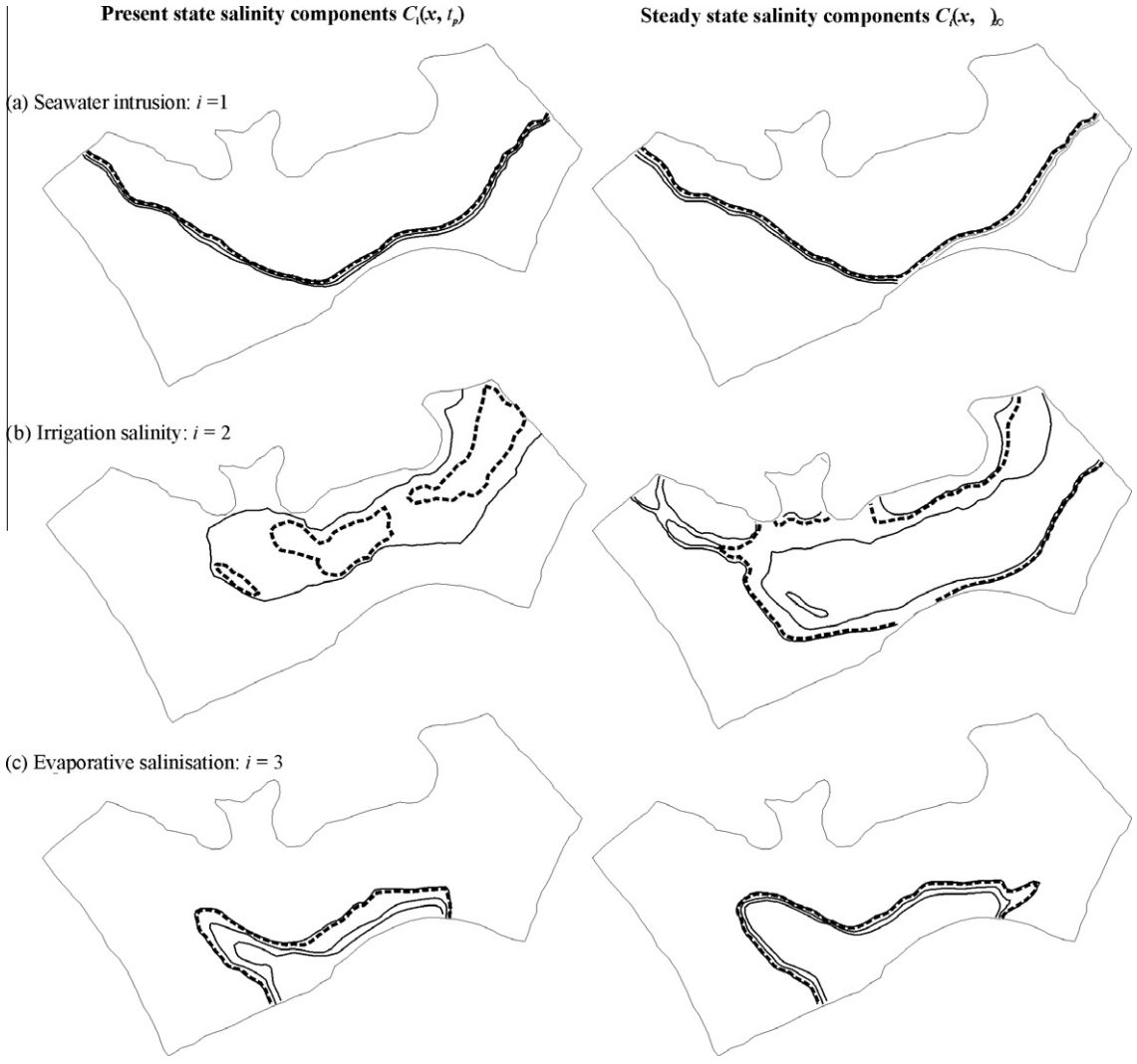

Fig. 12. Left column: salinisation components for present state $C_i(\boldsymbol{x}, t_p)$; Right column: 'quasi'-steady-state salinisation components $C_i(\boldsymbol{x}, \infty)$. Rows: a) Seawater intrusion components (i = 1); b) Irrigation salinisation components (i = 2) and c) Evaporative salinisation components (i = 3). Same iso-contours as in Fig. 10 and Fig. 11, with the iso-contour 2 mS/cm shown as bold stippled line.

5.3. Simulation of the salinity components $C_B(\boldsymbol{x}, \infty)$, $C_i(\boldsymbol{x}, t_p)$ and $C_i(\boldsymbol{x}, \infty)$

In this section, the simulations of all the required salinity components for the risk assessment procedure are described, starting with the bulk steady-state salinity distribution, followed by the decomposition into the three identified salinity components.

5.3.1. Simulation of the 'quasi' steady-state bulk salinity distribution $C_B(\boldsymbol{x}, \infty)$

The first component for the risk index definition to be simulated is the bulk salinity distribution at steady-state $C_B(\boldsymbol{x}, \infty)$. Due to the problem arising from the evaporative salinity accumulation, leading to infinitely high concentrations at steady-state, simulation was carried out for 50,000 days, yielding the 'quasi' steady-state bulk salinity component $C_B(\boldsymbol{x}, \infty)$, shown in Fig. 11b. Running the 'quasi'-steady-state simulation over a time-span of 50,000 days was found to be an adequately long time-period. Salinities throughout the system were stabilised apart from the concentrations in the area close to the salt lake, some of which were still rising. The concentration evolution is shown on the graphs for selected positions in the aquifer in Fig. 11. Inland and coastal observation points can be seen to be stabilised after 50,000 days, while some observation points in the salt lake area still increase, even beyond the limit of solubility (dashed line, indicating the relative concentration corresponding to the limit of solubility). Simulation should necessarily be stopped at this stage, since such high salinities will artificially affect the density-dependent flow and transport conditions with concentrations that are physically meaningless. This 'quasi'-steady-state approach may also be justified by the fact that comparing the present state situation with a situation 140 years ahead is sufficiently long, not only with respect to the stability of the hydraulic situation over time, but also with respect to the time-frame for which management schemes are designed.

5.3.2. Decomposition into salinity components $C_i(\boldsymbol{x}, t_p)$ and $C_i(\boldsymbol{x}, \infty)$

Since decomposition of the bulk salinity distributions into salinity components is based on the principle of linear superposition, the interdependencies of the three salinisation processes in the Akrotiri aquifer require approximations of the applicability of this basic assumption.

The first approximation that is made, is that salinity induced by irrigation/agriculture, being an order of magnitude smaller than the other salinisation processes, does not affect density-dependent flow, and can therefore be decoupled from the seawater and

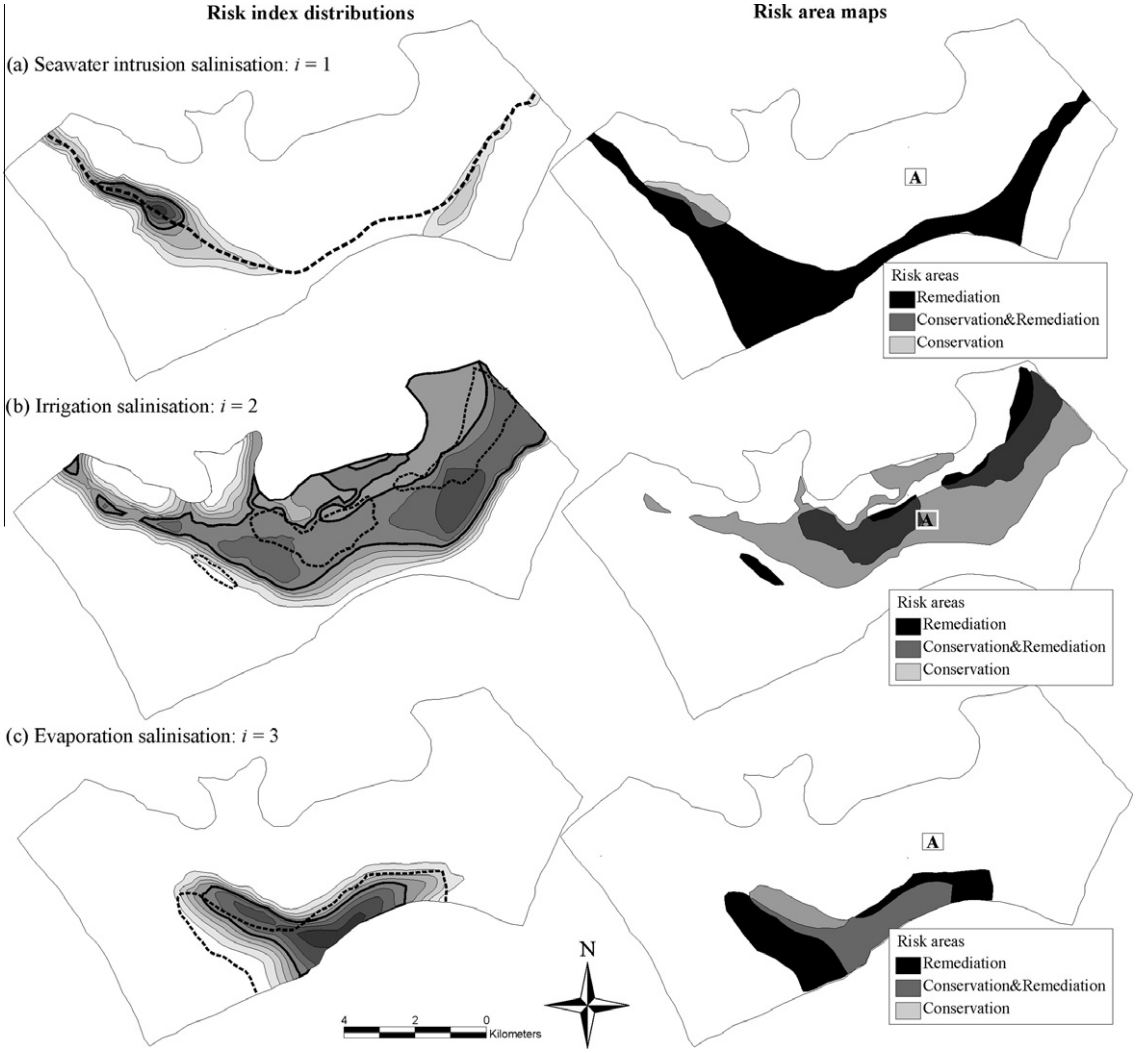

Fig. 13. Left column: Risk index distributions $R_i(\boldsymbol{x})$ within the gravel layer: iso-contour interval 0.1, critical risk index value $R_C = 0.5$ shown as bold line, threshold salinity C_T-contour as stippled bold line. Right column: risk area maps obtained from criteria in Table 2 with indicated management requirements. Rows: (a) Seawater intrusion ($i = 1$); (b) Irrigation salinisation ($i = 2$); (c) Evaporative salinisation ($i = 3$). Zone **A** is indicated on the risk area maps: location where several hectares of orange trees died due to inappropriate management scheme.

evaporative salinisation component. This allows direct simulation of the irrigation/agriculturally induced salinisation component.

The second hypothesis is that seawater intrusion does not depend on the evaporative salinisation component. This is strictly speaking not the case, since seawater movement, as it advances towards the salt lake, will be influenced by the presence of the highly saline groundwater there. However, since it mainly affects the area close to the salt lake, the result of the risk map in that particular area will have to be interpreted with reluctance.

The third assumption which is made, to obtain the evaporative salinisation component, is that the sum of all salinity components adds up to the bulk salinity distribution, as suggested by Eq. (2). The evaporative salinity component cannot be simulated separately, since it entirely depends on solutes already present in the system. Hence, deducing the seawater intrusion and irrigation-induced salinity components from the bulk salinity components yields an acceptable approximation of the evaporative salinity component.

5.3.2.1. Simulation of the seawater intrusion components (i =1). The seawater intrusion components were simulated by constant concentration boundary conditions on the seafloor ($C = 1$). The freshwater limits along the inland boundaries remained unchanged (with $C = 0.02$). The solute source term on the irrigated fields was deactivated (set to zero) and the evaporative fluid sink leading to solute accumulation by evaporative process was replaced by an outward-directed fluid flux boundary condition, allowing complete evacuation of the solutes along this area. The simulation was first run for the time-span 1986–2003 to obtain the present state component $C_1(\boldsymbol{x}, t_p)$ and then run for another 50,000 days to obtain the 'quasi'-steady-state-component $C_1(\boldsymbol{x}, \infty)$, shown in Fig. 12a.

5.3.2.2. Simulation of the irrigation salinity component (i =2). The irrigation salinity component was obtained by assigning a concentration of $C = 0$ on the all other inflowing boundaries. The evaporative processes were again simulated by an outward directed flux boundary condition to allow evacuation of the solutes and an initial concentration of $C = 0$ was used, assuming that irrigation salinisation only started after 1986. Again, the simulation was first run for the time-span 1986–2003, yielding the present state irrigation salinity component $C_2(\boldsymbol{x}, t_p)$ and then for additional 50,000 days to obtain the 'quasi'-steady-state component $C_2(\boldsymbol{x}, \infty)$, shown in Fig. 12b.

5.3.2.3. Evaporative salinity component (i = 3). As mentioned, the evaporative salinity component cannot be simulated separately, since it entirely depends on the primary salinisation processes. Assuming that Eq. (2) is valid in most parts of the domain allowed deduction of the seawater and irrigation salinity components, respectively, from the bulk salinity components, yielding the remaining evaporation salinity components $C_3(\boldsymbol{x}, t_p)$ and $C_3(\boldsymbol{x}, \infty)$, shown in Fig. 12c.

Fig. 12 shows all the salinity components of the three salinisation components. Adding up the present state and the 'quasi'-steady-state components, respectively, yields the bulk salinity components shown in Fig. 11.

5.4. Risk mapping of the Akrotiri aquifer

To establish the risk index and risk area maps for the Akrotiri area, use was made of the salinity components shown in Fig. 12 and Eq. (1) was applied in a map overlay principle.

The risk indices were calculated for all coordinates in the gravel layer, yielding a 2D representation of the risk index distributions, although these maps can be made for any of the aquifer horizons. On the left-hand side of Fig. 13, the risk index distributions of the three salinisation components are shown (grey scale with 0.1 iso-contour intervals and the iso-contour 0.5 shown in bold), as obtained from solving Eq. (1). The concentration contour of the present state threshold concentration of each component is defined here as $C_T = 2$ mS/cm and is shown as stippled bold line, projected onto the risk index distributions. A critical risk index of $R_C = 0.5$ was defined. This implies that the electrical conductivity may in places double to 4 mS/cm, which is close to the limit of exploitability for citrus plantations. Overlaying the critical risk index contour with the respective critical threshold concentration allows definition of the risk areas, according to the criteria defined in Table 2, and is shown on the right hand side of Fig. 13 for each salinisation component: (a) seawater intrusion component, (b) irrigation salinity component and (c) evaporation salinity component.

5.4.1. Seawater intrusion risk areas

Fig. 13a shows the seawater intrusion risk index distribution and risk area map. Comparing it with the area identified as being dominated by seawater intrusion in Fig. 5 shows that the high risk area requiring remediation ($C_1(\boldsymbol{x}, t_p) > C_T$ and $R_1(\boldsymbol{x}) < R_C$, according to Table 2) corresponds to the area identified as seawater intrusion dominated based on hydrochemical investigations. The area requiring conservation and remediation is rather small ($C_1(\boldsymbol{x}, t_p) > C_T$ and $R_1(\boldsymbol{x}) > R_C$), indicating that seawater intrusion is close to steady-state conditions with respect to the 1986–2003 average hydraulic condition. In the central area of the aquifer, where groundwater salinisation has been believed to be caused by seawater intrusion, the risk of seawater intrusion is negligible ($C_1(\boldsymbol{x}, t_p) < C_T$ and $R_1(\boldsymbol{x}) = 0$, requiring no management action with respect to seawater intrusion).

5.4.2. Irrigation salinity risk areas

The dominant salinisation process in the central area is related to irrigated agriculture, and is nicely revealed in the risk index distribution and risk area map of the irrigation salinity components, shown in Fig. 13b. There is a central area requiring conservation and remediation ($C_2(\boldsymbol{x}, t_p) > C_T$ and $R_2(\boldsymbol{x}) > R_C$), surrounded by a vast area requiring conservation ($C_2(\boldsymbol{x}, t_p) < C_T$ and $R_2(\boldsymbol{x}) > R_C$). In this area, irrigation practices should be adopted which reduce the salt load: diminishing agrochemical additives or mixing of groundwater with different quality, as to homogenise the salt load on the irrigated surfaces.

5.4.3. Evaporative salinity risk areas

Fig. 13c shows the risk index distribution related to evaporative salinisation along the salt lake and extending towards the marshlands north-westward. Since salinities are very high in this area, a relatively large area would require remediation measures ($C_1(\boldsymbol{x}, t_p) > C_T$ and $R_1(\boldsymbol{x}) < R_C$), while the central area requires conservation and remediation ($C_1(\boldsymbol{x}, t_p) > C_T$ and $R_1(\boldsymbol{x}) > R_C$). A small area in the north-west requires conservation only ($C_1(\boldsymbol{x}, t_p) < C_T$ and $R_1(\boldsymbol{x}) > R_C$) and is probably the most relevant area to focus on, since remediation measures in the given setting are very hard to implement. In the area requiring remediation, surface drainage from the marshlands could be a possible action. However, as mentioned, the salinity risk areas for the evaporative salinity components may be biased due to the assumption that was made that seawater intrusion is independent of this component. Particularly in the area between the salt lake and the sea these maps should not be over-interpreted.

Comparing the different risk area maps in Fig. 13 with each other shows that the different salinisation processes are spatially very variable, calling for different management actions in different areas of the aquifer.

The area indicated in Fig. 13 as **A** is the approximate zone where several hectares of orange trees died within few weeks after an exceptionally wet winter in 2003/2004, as described in Section 5.1, due to a rising water table and salt accumulation in the root zone. As can be seen from Fig. 13a, the risk of seawater intrusion in the area **A** is negligible but irrigation-induced salinisation is the most important salinisation process, requiring conservation and remediation measures in that area. Hence, with such risk area, decision makers can adopt and design a process-based management scheme, accounting for the spatial variability of the dominant processes.

Such risk area maps can of course also be established for modified hydraulic conditions, e.g. to test the potential impact of new artificial infiltration ponds or new extraction patterns. This simply implies simulation of all steady-state components according to the modified hydraulic conditions, indicating the new direction towards which the system is heading. In such cases, even negative risk indices can be obtained, which are a clear indication of groundwater quality amelioration (i.e. steady-state salinity lower than the present state salinity), as pointed out in Table 2. New hydraulic conditions should therefore be designed to produce a maximum of negative risk indices.

6. Discussion and conclusions

The presented framework for a salinisation risk assessment methodology allows process-based identification of the spatial variability of different salinisation processes, provided the salinisation processes have been correctly identified by field investigations and a numerical flow and transport model has been well calibrated.

The risk area maps resulting from this methodology are a promising tool for the design of groundwater management schemes. They condense relevant information from complex dynamic processes obtained from numerical simulations and visualise the results in simple and static maps, accessible to decision makers who are not familiar with groundwater dynamics. However, the results of the presented methodology entirely depend on the numerical model and its calibration, which, again, may be biased by the chosen modelling approach.

Authorities or decision-makers may not be willing to invest in a numerical model to obtain risk area maps for management purposes only. However, if a numerical model of an area is elaborated where several salinisation processes are superimposed, the presented approach can very easily be suggested as a separate package, requiring very little additional effort.

The restrictions which are related to the assumption of linear superposition of different fractions with different salinities have to be carefully evaluated for any real case study. If density-driven flow can be shown to be dominant, or if secondary salinisation components cannot be decomposed, the approach may not be applicable. These issues have to be kept in mind during the risk assessment procedure, since Eq. (2) is no longer strictly speaking correct, at least not everywhere in the domain. In any real-case site, sensible assumptions addressing these difficulties have to be made to allow approximation of the relationship given in Eq. (2), which is the key to the proposed framework.

Although the assumptions may be restrictive in some areas, the fact that the results are used for regional mapping purposes alleviate the draw-backs. The risk area maps are not intended to be used for any exact prediction of solute evolutions at any particular location, but indicate spatial variability of salinisation risk related to different processes. Hence, the risk assessment relates to a sub-regional scale (kilometre-scale) rather than to a local observation-well scale. In the example of the Akrotiri aquifer, the lateral versus vertical aquifer extent is such that it can be considered as a sheet. Therefore, the impact of density-driven flow and transport on the regional scale is damped. In real-case sites with considerable aquifer thicknesses, i.e. aquifers which do not have a 'sheet-like' geometry, the proposed mapping procedure should not be applied.

In the example of the Akrotiri aquifer, the risk area maps reveal high salinisation risk in the central area of the aquifer caused by irrigation-induced salinisation. In reality, this area has been managed in the belief that seawater intrusion is the dominant process. Such risk area maps could therefore be a positive basis to re-evaluate the present groundwater management scheme. Since the Akrotiri aquifer and its seawater-intrusion focalised management scheme are believed to be quite representative of many coastal aquifers around the Mediterranean region, the presented salinisation risk assessment could be a possible starting point to review the design of management strategies.

Acknowledgements

The field work carried out and the data retrieved to elaborate the numerical model could only be done due to the close collaboration with the Cyprus Water Development Department, in particular Dr. A. Christodoulides. The author thanks Pierre Perrochet, Fabien Cornaton and Philippe Renard for fruitful discussions. The constructive comments from two anonymous reviewers were very much appreciated and considerably improved the manuscript. The research described in this paper was sponsored by the European Community project SWIMED, Contract Nr. ICA3-CT-2002-10004 and also by the Swiss National Science Foundation post-doctoral Grant, No. PBNE2-110374.

References

Aller, L., Bennet, T., Lehr, J. H., Petty, R. J., 1987. DRASTIC: A Standardised System for Evaluating Groundwater Pollution Potential Using Hydrologic Settings. US EPA Report 600/2-87/035, Robert S. Kerr Environmental Research Laboratory, Ada, OK.

Civita, M., De Rigibus, C., 1995. 'Sperimentazione di alcune metodologie per valutazione della vulnerabilità degli aquiferi. Q Geol Appl. Pitagora Bologna 3, 63–71.

Connell, L.D., van den Daele, G., 2003. A quantitative approach to aquifer vulnerability mapping. Journal of Hydrology 276, 71–88.

Constantinou, C., 1970. Hydrogeology of the Akrotiri Peninsula, Cyprus. Geological Survey Department, Nicosia.

Custodio, E., 1997. Studying, monitoring and controlling seawater intrusion in coastal areas. Guidelines for Study, Monitoring and Control, FAO Water Reports, vol. 11, no. 1, pp. 7–23.

Diersch, H.J., 2007. FEFLOW Reference Manual 5.3. WASY Institute for Water Resources Planning and Systems Research Ltd., Berlin.

Doerfliger, N., Zwahlen, F., 1997. 'EPIK: a new method for outlining of protection areas in karstic environments'. In: Günay, G., Johnson, A.I. (Eds.), International Symposium and Field Seminar on Karst Waters and Environment Impacts. Antalya, Balkema, Rotterdam, pp. 177–223.

Foster, S.S.D., 1987. Fundamental concepts in aquifer vulnerability, pollution risk and protection strategy. In: Van Duijevenboden, W., Van Waegeningh, H.G. (Eds.), Vulnerability of Soil and Groundwater to Pollutants, TNO Committee on Hydrogeological Research, Proceedings and Information, vol. 38, The Hague, pp. 69–86.

Gogu, R.C., Dassargues, A., 2000. Current trends and future challenges in groundwater vulnerability assessment using overly and index methods. Environmental Geology 39 (6), 549–559.

Helm, P., 1996. Integrated risk management for natural and technological disasters. Tephra 15 (1), 4–13.

Jackovides, J., 1982. Southern Conveyor Project, Feasibility study. Groundwater Resources (3), Cyprus Water Development Department, Nicosia.

Kitching, R.A., 1975. A Mathematical Model of the Akrotiri Plio-Pleistocene Gravel Aquifer, Cyprus. IGS, RN 75/2, London.

Konikow, L.F., Person, M., 1985. Assessment of long-term salinity changes in an irrigated stream-aquifer system. Water Resources Research 21 (11), 1611–1624.

Marshall, J.K., Morgan, A.L., Akilan, K., Farell, R.C.C., bell, D.T., 1997. Water uptake two river red gum (*Eucalyptus camaldulensis*) clones in a discharge site plantation in the Western Australien wheatbelt. Journal of Hydrology 200 (1.4), 136–148.

Meilhac, C., 2003. Hydrogeological and Geochemical Investigation of the Akrotiri Aquifer, Cyprus. Master thesis, Formation postgrade en hydrologie et hydrogéologie, Specialisation hydrogéologie, Université de Neuchâtel.

Milnes, E., 2000. Hydrogeological Investigation of the Akrotiri Porous Aquifer, Southern Cyprus: Seawater intrusion modelling. Diploma Thesis, Cycle postgrade interuniversitaire EPFL et Université de Neuchâtel (Switzerland).

Milnes, E., 2005. Modelling Groundwater Salinisation in Irrigated Coastal Areas: from Solute Recycling Concepts to Quantitative Risk Assessment. PhD Thesis, University of Neuchâtel (Switzerland).

Milnes, E., Perrochet, P., 2006. Direct simulation of solute recycling in irrigated areas. Advances in Water Resources 29 (8), 1140–1154.

Milnes, E., Renard, P., 2004. The problem of salt recycling and seawater intrusion in coastal irrigated plains: an example from the Kiti aquifer (Southern Cyprus). Journal of Hydrology 288, 327–343.

Milnes, E., Meilhac, C., Yeo, D., Renard, P., Hunkeler, D., Schnegg, P., Bourret F., 2006. Hydrogeochemical and hydrogeological investigation in the Akrotiri aquifer: identification of multiple salinisation processes and implementation criteria for monitoring networks. In: Proceedings of the 1st SWIM-SWICA Conference, Cagliary.

Pearce, M.W., Schumann, E.H., 2001. The impact of irrigation return flow on aspects of the water quality of the Upper Gamtoos Estuary, South Africa. Water SA 27 (3), 367–372.

Reading, H.G., 1986. Sedimentary Environments and Facies. Blackwell Scientific Publications, ISBN 0-632-01223-4.

Richter, B.C., Kreidtler, B.E., 1993. Geochemical Techniques for Identifying Sources of Groundwater Salinisation. C.K. Smoley, ISBN 1-56670-000-0.

Ruppert, M.G., 2001. Calibration of the DRASTIC ground water vulnerability mapping method. Ground Water 39 (4), 625–630.

Sites, W., Kraft, G.J., 2000. Groundwater quality beneath irrigated vegetable fields in a north-central US sand plain. Journal of Environmental Quality 29 (5), 1509–1517.

Sophocleous, M., Ma, T., 1998. A decision support model to assess vulnerability to salt water intrusion in the Great Bend Prairie aquifer, Kansas. Groundwater 36 (3), 476–483.

Steward, I.T., Loague, K., 1999. A type transfer function approach for regional-scale pesticide leaching assessments. Journal of Environmental Quality 28, 378–387.

Thorntwaite, C.W., Mather, J.R., 1955. Publications in Climatology. Centerton, New Jersey Dexel Institute of Technology, Laboratory of Climatology, vol 8, no. 1, ISBN4035048.

Vengosh, A., Rosenthal, E., 1994. Saline groundwater in Israel: its bearing on the water crisis in the country. Journal of Hydrology 156, 389–430.

Vengosh, A., Spivack, A., Artzi, Y., Avner, A., 1999. Geochemical and boron, strontium and oxygen isotopic constraints on the origin of the salinity in groundwater from the Mediterranean coast of Israel. Water Resources Research 35 (6), 1877–1894.